Nanoscale stress distributions and microstructural changes at scratch track cross-sections of a deformed brittle-ductile CrN-Cr bilayer

M. Meindlhumer, J. Zalesak, W. Ecker, M. Rosenthal, S. Niese, P. Gawlitza, H. Hruby, C. Mitterer, R. Daniel, J. Keckes, et al.

Materials and Design 195 (2020) 109023

Contents lists available at ScienceDirect

Materials and Design

journal homepage: www.elsevier.com/locate/matdes

Nanoscale stress distributions and microstructural changes at scratch track cross-sections of a deformed brittle-ductile CrN-Cr bilayer

M. Meindlhumer [a,*], J. Zalesak [b], W. Ecker [c], M. Rosenthal [d], S. Niese [e], P. Gawlitza [f], H. Hruby [g], C. Mitterer [h], R. Daniel [a], J. Keckes [b,h], J. Todt [b]

[a] Christian Doppler Laboratory for Advanced Synthesis of Novel Multifunctional Coatings at the Department of Materials Science, Montanuniversität Leoben, Leoben, Austria
[b] Erich Schmid Institute for Materials Science, Austrian Academy of Sciences, Leoben, Austria
[c] Materials Center Leoben Forschung GmbH, Leoben, Austria
[d] ESRF, Grenoble, France
[e] AXO Dresden GmbH, Dresden, Germany
[f] Fraunhofer Institute for Material and Beam Technology IWS, Dresden, Germany
[g] voestalpine eifeler Vacotec GmbH, Düsseldorf, Germany
[h] Department of Materials Science, Montanuniversität Leoben, Leoben, Austria

HIGHLIGHTS

- Experimentally determined multi-axial residual stress distributions across a scratched Cr-CrN bilayer film reveal deformation mechanisms.
- The ductile Cr sublayer provides toughening through plastic deformation while the hard/brittle CrN toplayer absorbs severe stresses, functioning synergistically.
- Small-angle X-ray scattering and X-ray peak width analyses elucidate microstructural changes unaccounted for by finite element modelling.

GRAPHICAL ABSTRACT

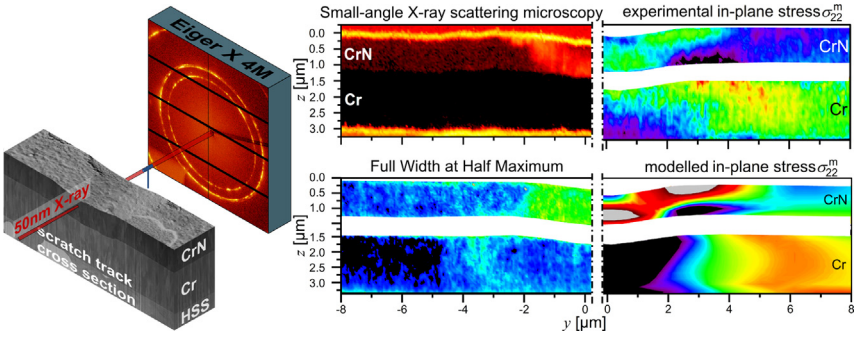

ARTICLE INFO

Article history:
Received 22 June 2020
Received in revised form 30 July 2020
Accepted 31 July 2020
Available online 05 August 2020

Keywords:
CSnanoXRD
Scratch testing
Thin films
Cr
CrN

ABSTRACT

In order to interpret the mechanical response of thin films subjected to scratch tests, it is necessary to elucidate local stress distributions and microstructural changes accompanying deformation across the scratch track area. Here, 50 nm synchrotron cross-sectional X-ray nanodiffraction and electron microscopy are used to characterize nanoscale multiaxial residual stress gradients and irreversible microstructural-morphological changes across a brittle-ductile film consisting of 1.2 and 2 μm thick CrN and Cr sublayers. The experimental results reveal a complex alternation of the original columnar grain microstructure and a formation of pronounced lateral and depth stress gradients, which are complemented by a finite element model. After scratching, steep gradients of in-plane, out-of-plane and shear stress distributions were revealed, ranging from −6 to 1.5 and − 1.5 to 1.5 GPa in CrN and Cr, respectively, which are furthermore correlated with microstructural changes and residual curvatures. The scratch test results in intergranular grain sliding and the formation of nanoscopic intragranular defects within CrN, while Cr sublayer's thickness reduction and pile-up formation are accompanied by a bending of columnar crystallites and localized plastic deformation. In summary, the quantitative stress data elucidate the stabilizing role of the Cr sublayer, which suppresses the bilayer's catastrophic fracture during scratch tests.

* Corresponding author.
E-mail address: michael.meindlhumer@unileoben.ac.at (M. Meindlhumer).

https://doi.org/10.1016/j.matdes.2020.109023

1. Introduction

Scratch testing was developed to investigate the adhesion behaviour of hard ceramic thin films on various types of substrates and is nowadays widely used in research and technology [1,2]. Subsequent works indicated that a great variety of intrinsic (sample) and extrinsic (method-related) parameters, such as film and substrate mechanical properties, surface roughness, indenter radius (typically 200 μm), applied loads (up to 100 N) and scratching velocity can critically alter the observed scratch behaviour, shifting the failure mode from a film-substrate interface adhesion-dependent regime to a mode where deformation/cohesive strength of the film itself is decisive [3,4]. Bull et al. distinguished between adhesion and deformation/cohesive strength-related film failures using scanning electron microscopy (SEM) analysis and established classification rules for these two types of regimes [5,6]. Especially in the case of well-adhering films, rather the cohesive strength of the film and its ability to deform plastically is of higher relevance for its resistance against scratching [4,7,8]. Further miniaturization of instruments led to the development of the nanoscratch test, where applied loads are in the range of 1–500 mN, using indenter tip radii of 1–20 μm, yielding the possibility to test films by scratching without interference from the substrate [7,9–11] or even to quantify adhesion [12]. Similar to nanoindentation with a spherical indenter, also in the case of scratch testing, bending of the hard nanoceramic thin film into the plastically deformable substrate may, however, predetermine the indenter's imprinting and/or sliding behaviour [13–16]. In terms of scratch testing, the nanoscratch method has become an important tool for the characterization of nanoscale wear and friction behaviour during single asperity contact [7].

For thin films, special interest was devoted to the experimental scratch analysis of brittle-ductile multilayers. Fontalvo et al. [14] analysed the crack behaviour of CrN-Cr bilayered thin films with an overall thickness of 3 μm, where the incremental increase of ductile Cr interlayers thickness led to a reduction of wear by an order of magnitude, despite the fact that the remaining thickness of the hard CrN toplayer was decremented accordingly. As indicated also by an ex-situ analysis of indentation data from the brittle-ductile CrN-Cr model system in Refs. [17, 18], the introduction of thin Cr interlayers has a significant influence on the crack propagation behaviour and on the overall mechanical stability of CrN-Cr multilayers. Ductile Cr interlayers and CrN-Cr interfaces operate as crack blunting and deflection barriers, increase the multilayer's resistance against catastrophic fragmentation and serve as a stabilizing component, preventing also rupture and delamination of the film from the substrate [16,18–20].

Significant attention has been devoted to the analysis of stress-strain distributions across scratched materials, both experimentally and using theoretical approaches at different length scales. Recent studies of Brinckmann et al. on coarse-grained bulk austenitic steel revealed that the complex multi-axial stress distribution introduced during scratching results in the activation of multiple slip systems within the near-surface crystallites, depending on their crystallographic orientation [21,22]. Pioneering experimental work on the evaluation of stress distributions across scratched surfaces has been reported by Khan et al. [23], who investigated scratches in Al alloys by synchrotron X-ray microdiffraction with a spatial resolution of ~50 μm, after scratching using two different types of tools. Consequently, two different types of residual stress distributions were induced, as a result of “ploughing” and “cutting” modes, where the former is more similar to scratching and resulted in residual stress concentrations of ~80% higher compared to the latter [23]. Currently, however, the state-of-the-art experimental studies [24] on the scratch behaviour of nanocrystalline thin films suffer from poor spatial resolution, which does not allow for the determination of complex multiaxial stress-strain concentrations at the submicrometre scale.

Finite element modelling (FEM) has been the primary approach of assessing local stress and strain distributions during and after scratch tests on thin films [25–27]. Holmberg et al. [26] analysed stress distributions within a TiN film on high-speed-steel (HSS) during scratching with a conventional Rockwell indenter under a load of 20 N using displacement-controlled FEM. They reported principal stress magnitudes up to 3 GPa besides the scratch path and up to −1.75 GPa directly under the indenter tip. The main drawback of state-of-the-art FEM studies is, however, the missing possibility to experimentally verify the modelled stress-strain distributions at the nanoscale.

Since 2012, cross-sectional X-ray nanodiffraction (CSnanoXRD) has been continuously developed and proven to be successful in determining cross-sectional phase, microstructure and stress-strain gradients with a spatial resolution down to ≤30 nm [28]. Furthermore, CSnanoXRD is not only capable to resolve the aforementioned gradients, cf. for example [29–32], but ex-situ and in-situ studies on thin films subjected to nanoindentation [17,33,34] revealed great potential for the quantification of nanoscale multiaxial stress-strain distributions.

In this work, two dimensional (2D) residual stress distributions and microstructural changes are experimentally characterized at cross-sections of a bilayered brittle-ductile nanocrystalline CrN-Cr film on steel substrate by CSnanoXRD and electron microscopy techniques. The observed correlations between the nanoscale multiaxial stress distributions and the microstructural changes at scratch track cross-sections allow for elucidating elasto-plastic deformation mechanisms separately for the brittle and the ductile columnar-grained sublayers, which are further complemented by FEM numerical simulation.

2. Experimental

2.1. CrN/Cr thin film synthesis

For this study, a bilayer film consisting of a 1.2 μm thick CrN toplayer and a 2 μm thick Cr sublayer was deposited on an electrolytically polished planar HSS plate with lateral dimensions of 20 × 20 mm and a thickness of 2 mm. The film was deposited in a static mode by unbalanced reactive direct current magnetron sputtering using a powder-metallurgically produced Cr target at 350 °C and a total pressure of 1 Pa. Prior to the deposition process, the chamber was evacuated to 10^{-4} Pa, the substrate was then heated to 350 °C and Ar plasma etched for 10 min. At first, the Cr sublayer was deposited in a pure Ar atmosphere and an applied substrate bias voltage of −40 V, whereas the CrN toplayer was grown in an Ar + N_2 atmosphere at a N_2 partial pressure of 0.25 Pa and a substrate bias voltage of −80 V.

2.2. Scratch testing

Scratch tracks investigated in this work were produced at constant loads in order to generate relatively homogenous stress fields along the tracks. Therefore, a set of five scratch tests was performed on the surface of the planar CrN/Cr/HSS sample in a Fischer-Cripps Laboratories UMIS nanoindenter equipped with a sphero-conical diamond indenter with a tip radius of 5 μm using constant indenter loads of 100–500 mN, in steps of 100 mN and mutual distance of ~2 mm. The length of the scratches was set to 1 mm, while the indenter tip progressed with 100 μm/s. Surface morphologies of the scratches were then evaluated using SEM. Afterwards, the two scratches produced using indenter loads of and further denoted as *200 mN scratch track* and *400 mN scratch track*, which showed either no significant cracking or multiple cracking of the top CrN toplayer, respectively, were selected for further CSnanoXRD analysis.

2.3. Sample preparation

The scratched CrN/Cr/HSS sample was cut perpendicularly to the scratch tracks and then polished to a thickness of ~20 μm mechanically and using a focused ion beam (FIB) workstation in order to produce a cross-sectional synchrotron lamella (Fig. 1). According to Stefenelli

et al. [35], changes in the residual stresses due to preparation can be neglected, when maintaining a lamella thickness at least 5 times larger than the film thickness. FIB machining was performed in a ZEISS LEO 1540 CrossBeam Workstation using Ga^+ ions with a current of 100 pA. After the CSnanoXRD experiment, a ~500 nm thick tungsten protection layer was deposited onto the surface of the two scratch tracks (200 and 400 mN) using the gas injection system of the FIB workstation to protect the scratch track surface from the Ga^+ ion-damage. Afterwards the cross-sections were polished applying decreasing ion currents of 50 and 20 pA in order to reveal cross-sectional morphological features such as cracks, grain reorientation and plastic deformation within the two scratch track areas. Additionally, a FEI Helios NanoLab 660 FIB microscope was used for fabrication of electron-transparent specimens of the scratch track areas. Positions for lift-outs of lamellae were carefully chosen in order to contain the scratch imprints. In order to prepare the lamellae, the FIB was operated at stepwise reduced accelerating voltages from 30 to 2 kV and currents from 20 nA to 50 pA, respectively. The bright field (BF) scanning transmission electron microscope (STEM) micrographs were taken using a JEOL 2200FS operated at an accelerating voltage of 200 kV using a spot size of approx. 0.7 nm. Transmission Kikuchi Diffraction (TKD) was performed in the SEM on a Bruker QUANTAX EBSD analysis system suited for TKD on TEM samples using an accelerating voltage of 30 kV.

2.4. CSnanoXRD analysis

CSnanoXRD experiments were performed at the ID13 beamline of The European Synchrotron (ESRF) in Grenoble, France [28]. A pair of multi-layer Laue lenses (MLLs) [36] working with vertical and horizontal focal sizes of 50 and 35 nm (along z and y directions in Fig. 1) and a focal depth of ~20 μm were used to focus the X-ray beam with a photon energy of 12.7 keV [28]. Prior to the CSnanoXRD experiment, the interface between the CrN toplayer and Cr sublayer was aligned parallel to the incident X-ray beam direction at two cross-sectional sample y positions (corresponding to the respective 200 and 400 mN scratch track areas) by performing a set of vertical absorption line-scans along the z axis at various sample φ orientations (Fig. 1) using a passivated, implanted, planar silicon diode detector to measure transmitted X-ray intensities [17,28]. The two optimal sample orientations were determined by maximizing the absorption contrast between the CrN toplayer and the Cr-sublayer. Subsequently, 2D absorption scans (presented in Suppl. Fig. 1) were performed to locate the scratch track areas and to determine the centres of the CSnanoXRD mesh scans.

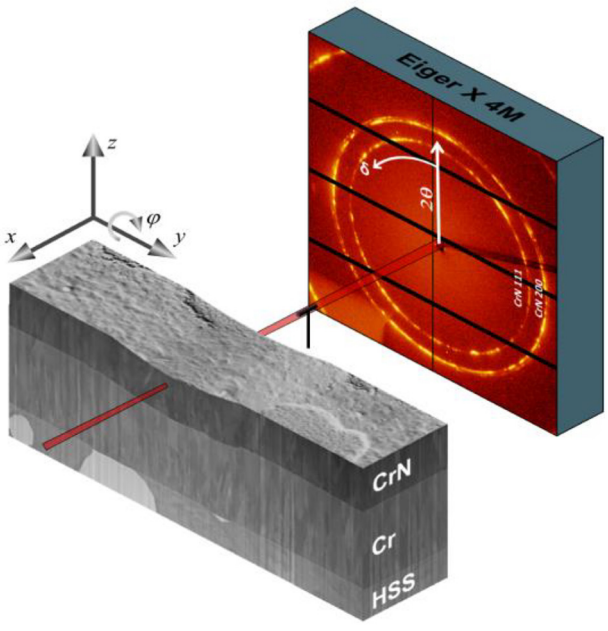

Fig. 1. A schematic description of the CSnanoXRD experiment. A thin lamella with dimensions of ~0.02 × 5 × 2 mm^3 was scanned in an X-ray beam with dimensions of ~50 × 35 nm^2 along y and z axes using steps of 50 nm. 32,421 and 26,361 2D diffraction patterns were recorded on an Eiger X 4 M CCD detector from (16 × 5) and (13 × 5) μm² large scratch tracks' cross-sections, prepared at loads of 200 and 400 mN, respectively.

The two mesh scan areas of (16 × 5) μm² and (13 × 5) μm² at the positions of the 200 and 400 mN scratches, respectively, were scanned by moving the sample stepwise along the y *and* z axis direction using 50 nm steps. The 2D diffraction signal was recorded by a Dectris Eiger X 4 M detector at each measurement position using an acquisition time of 50 ms. Altogether, 32,421 and 26,361 2D diffraction patterns were recorded at the two respective scratch track areas. Additionally, line scans with a resolution of 20 nm were performed at presumed points of interest throughout the sample and were used for detailed texture analysis. The exact detector geometry with respect to the sample was calibrated using a NIST corundum powder. The sample-to-detector distance was evaluated as 129.81 mm. Evaluation of 2D diffraction patterns containing CrN 111 and 200 or CrN 110 Debye-Scherrer (DS) rings (Fig. 1) was performed using the pyFAI software package [37,38]. The unstressed lattice constant of $a_0^{\mathrm{CrN}} = 0.416691$ nm was determined from CrN 111 and 200 DS rings collected at the surface of an undeformed CrN film region, considering the stress-free out-of-plane film orientation [39]. For the evaluation of strain from Cr 110 DS rings, a lattice constant of $a_0^{\mathrm{Cr}} = 0.28839$ nm was adopted from literature [40], because no stress-free orientation could be determined due to the absence of a free Cr sublayer surface. The evaluation of in-plane $\sigma_{22}^m(y,z)$, out-of-plane $\sigma_{33}^m(y,z)$ and shear $\sigma_{23}^m(y,z)$ stress distributions in both phases (m) was performed using the approach from Ref. [33] (cf. also Supplementary Material). X-ray elastic constants $S_1^{m,\ hkl}$ of $S_1^{\mathrm{CrN},111} = -9.23 \times 10^{-4}\mathrm{GPa}^{-1}$, $\frac{1}{2}S_2^{\mathrm{CrN},111} = 4.446 \times 10^{-3}\mathrm{GPa}^{-1}$, $S_1^{\mathrm{CrN},200} = -2.99 \times 10^{-4}\mathrm{GPa}^{-1}$, $\frac{1}{2}S_2^{\mathrm{CrN},200} = 2.575 \times 10^{-3}\mathrm{GPa}^{-1}$, $S_1^{\mathrm{Cr},200} = -7.49 \times 10^{-4}\mathrm{GPa}^{-1}$, $\frac{1}{2}S_2^{\mathrm{Cr},110} = 4.441 \times 10^{-3}\mathrm{GPa}^{-1}$ for CrN and Cr *hkl* reflections were adopted from literature [41,42].

2.5. Simulation

A three-dimensional (3D) FE model was set up by applying the finite element software package Abaqus [43], in order to model and interpret the localized deformation phenomena, which led to the experimentally observed multiaxial stress distributions within a 1 μm thick CrN toplayer followed by the 2 μm thick Cr interlayer and 17 μm of HSS substrate. The width, height and length of the model region were set to 30, 20 and 76 μm, respectively. A half-symmetry condition was applied at the boundary plane containing the scratch path and the normal displacement, as well as the displacements at all other boundary planes except the sample surface were restricted during modelling of the scratch test. In a subsequent relaxation step representing the state during stress measurement, only the rigid body modes of the sample were restricted and the symmetry assumption remained. The interaction between indenter and specimen was defined by means of a penalty-contact with finite sliding formulation and a Coulomb friction coefficient of 0.2. A total number of 92,075 3D hexaeder elements with linear shape functions (C3D8) were used to discretise the sample. The element size was varied from ~100 nm in the contact region to ~4 μm in outer regions. The indenter tip was modelled by 3470 discrete rigid body elements as a quarter sphere with a radius of 5 μm. Isotropic elasto-plastic behaviour was defined for all materials within the simulation. The Young's modulus of CrN was assumed as 490 GPa and the Poisson's ration as 0.21. The flow stress was set to increase piecewise linearly from initially 10 to 20 GPa at 1% and to 25 GPa at 5% plastic strain, initial yield was taken from [44]. For Cr, the Young's modulus was assumed as 300 GPa and the Poisson's ration as 0.3. The yield limit of Cr was assumed to be 2 GPa

with multi-linear hardening to 5 GPa and 5.5 GPa at 10% and 100% plastic deformation, respectively [40,45]. The Young's modulus for HSS was defined as 210 GPa, with an initial flow stress of 2.5 GPa and a flow stress of 3.5 GPa at 5% plastic strain. The Poisson's ration was set to 0.3. The high hydrostatic compression under the indenter tip allowed severe plastic deformation of the involved materials before damage initiation. Therefore, the flow curves are defined up to high plastic strains. An initially equibiaxial residual stress state was defined in the simulation, according to the evaluation of the CSnanoXRD experiment, with −3 GPa for CrN and − 1 GPa for Cr. Variations of the film thickness and an interface peak of residual stress in CrN were neglected in the simulation (experimental data are shown in Suppl. Fig. 2). The simulation consisted of 5 consecutive steps: (i) application of residual stress according to the evaluation of the CSnanoXRD experiment, (ii) application of the indenting/scratching force, (iii) 10 μm of sliding, (iv) withdrawal of the indenter and (v) relaxation due to cutting of the sample lamella. In the case of the 400 mN scratch, the crack formation during scratching was considered, for the sake of simplicity, as a pre-existing single crack with a length and a width of 1 and 15 μm in *z* and *x* directions, respectively, located 3 μm from the centre of the scratch path (for details cf. Suppl. Fig. 3). It should be noted, that the length of the crack is similar to the thickness of the CrN toplayer.

3. Results and discussion

3.1. Cross-sectional scratch track area morphologies

A detailed SEM analysis of the scratch cross-sections is presented in Figs. 3 and 5a,c. In general, the CrN-Cr bilayer possessed a typical columnar grain microstructure with V-shaped grains in both sublayers (Figs. 3a-c, 5a), and due to heteroepitaxial growth of CrN on Cr, a nucleation layer within the CrN toplayer was not formed (c.f. Figs. 3a-c,5c), in good agreement with literature [19,40].

In the groove of the *200 mN scratch track* (Figs. 2a, 5a), a slight compression of the Cr sublayer in the central area and very small symmetrical pile ups are visible, as indicated by the horizontal dotted line in Fig. 5a, whereas the thickness of the CrN toplayer appears to remain unchanged. Additionally, under the residual imprint region, there are no surface debris or cross-sectional cracks visible (Fig. 2a). Furthermore, Fig. 5a indicates additionally a change in the columnar grain microstructure, namely a bending and/or rotation of the columnar grains within both sublayers. The bending/bulging of Cr grains is observed also within complementary BF-STEM and TDK micrographs in Figs. 3a and 4a,

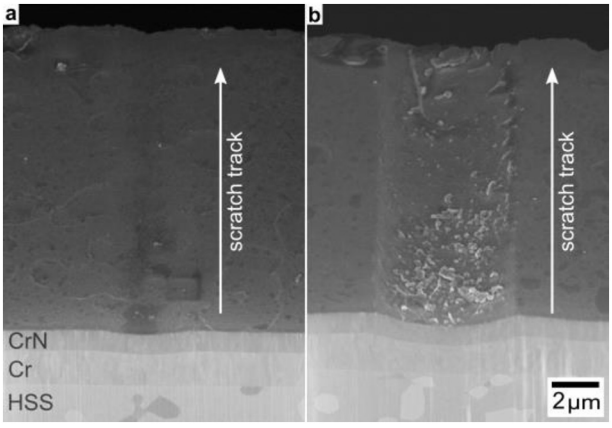

Fig. 2. SEM micrographs collected at an angle of 45 deg. with respect to the surface of the scratched CrN-Cr bilayer film on a HSS substrate. The scratch prepared using a load of 200 mN (a) left a residual imprint approx. 3 μm wide and 300 nm deep. The scratch prepared with a load of 400 mN (b) left a residual imprint approx. 5 μm wide and 800 nm deep, as measured from the top of the pile-up at the edge to the imprint centre.

respectively. Additionally, it should be noted that the number of grains within the investigated volume was too small to identify texture qualitatively, which will be discussed later in Sec. 3.4. In agreement with Ref. [14], pile-up formation and bulging is restricted to the Cr sublayer, whereas in the CrN layer only grain rotation takes place. An entirely different picture would be seen in a single-crystalline brittle material, like SiC, which has no ability of grain rotation or (bulk) plastic deformation, resulting in stress relaxation due to cracking outside the highly deformed zone, as reported in Ref. [46]. Here, the TEM analysis also revealed microscopic intergranular cracks starting from the film surface (Fig. 3b) and from the CrN-Cr interface (Fig. 3c) at the edge and in the centre of the scratch track, respectively. However, the cracks stop within the CrN toplayer (Fig. 3b,c). The associated relaxation of tensile stress will further be discussed in detail in Sec. 3.5.1. The groove of the *400 mN scratch track* shows an imprint depth of ~800 nm measured from the edge of the pile-up to the centre of the groove (Figs. 2b, 5c). The presence of microscopic surface debris on the imprint surface in Fig. 2b indicates a fragmentation of the CrN toplayer and material chipping, which is confirmed also by the cross-sectional intergranular cracks in Fig. 5c. Additionally, (i) the thickness of the Cr sublayer in the centre of the residual imprint is reduced from 2 to ~1.7 μm, whereas the thickness of CrN toplayer remains again unchanged (Figs. 2b,4,5c), (ii) pile-ups are formed in the Cr layer at the edges of the scratch groove (Figs. 2b,5c) and (iii) a rotation and/or a bending of the columnar grains in both materials can be observed in Figs. 3d, 4b and 5c, in agreement with the results from Refs. [15, 16, 18].

Moreover, BF-STEM and TKD micrographs shown in Figs. 3d,e and 4b confirm transgranular gliding of the columnar Cr grains approximately 250 nm beneath the CrN-Cr interface. This gliding is associated with the shearing of the columnar grains and the formation of a so-called dislocation trace line, which was also found in Cu during sliding contact at cryogenic temperatures [47–49]. Also, the bulging of Cr grains is more pronounced compared to those within the 200 mN scratch track (Fig. 3a). A pronounced bulging of the columnar grains is also found in CrN, as can be seen in Figs. 3e and 4b, which differs from the 200 mN scratch case, where only grain rotation was found in the CrN toplayer (Figs. 3a and 4a). Remarkably, the intergranular cracks formed during the scratch process penetrated through the entire CrN toplayer and stopped at the CrN-Cr interface (cf. Fig. 3d,e), in agreement with Ref. [18]. The cross-sectional intergranular crack formation in the brittle CrN toplayer is a consequence of the larger curvature caused by the deeper imprint (cf. Fig. 2) resulting in grain boundary sliding (Fig. 3e). The latter is promoted by the relatively small cohesive energy of the grain boundaries in nanoceramic CrN, as discussed elsewhere [45].

In general, it was observed that columnar grains of the CrN toplayer were oriented normal to the surface of the sliding indenter (towards it) after the scratch test (cf. Fig. 5). Contrary to this, the columnar grains of a monolithic TiN film from Ref. [33] indented with a sharp tip were reoriented parallel to the imprinting indenter facets (away from the imprint surface). While the former is attributed to plastic deformation of the underlying Cr sublayer, which allowed the CrN toplayer to adjust to the sliding indenter, the latter is interpreted mainly by a cleavage-like separation of the grains during the penetration of the layer by the indenter.

3.2. Small-angle X-ray scattering microscopy

Generally, diffuse X-ray scattering at relatively small diffraction angles (around the beam stop in Fig. 1) can be attributed to electron density variation originating from the presence of nanoscopic structural heterogeneities within the X-ray gauge volume. These may include nanoscale alternation of phases, presence of grain boundaries, interfaces, cracks, roughness of surfaces and interfaces, precipitates and pores with sizes of ~ λ/θ , where λ represents the X-ray wavelength and θ is the Bragg angle [30,50]. In the present case, the scattered signal on the 2D detector at the diffraction angles of ~0.1 to ~1 deg. in Fig. 1 was

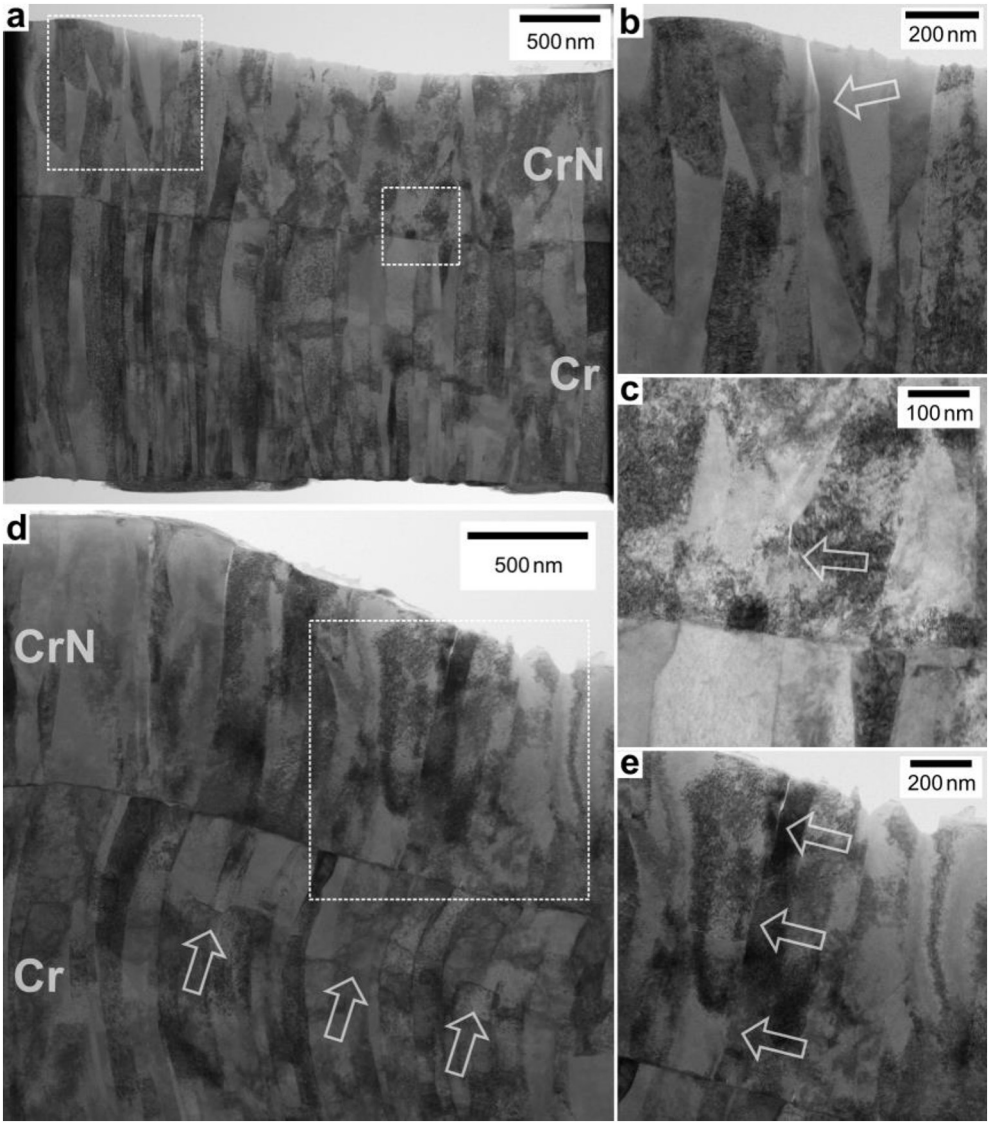

Fig. 3. BF STEM micrograph of the 200 mN scratch cross-section (a). The dashed regions marked in (a) are magnified in (b) and (c) and show cracks propagating along the columnar grain boundaries from the surface and from the CrN-Cr interface into the brittle CrN toplayer, respectively. STEM micrograph of the 400 mN scratch cross-section (d). The dashed region marked in (d) is magnified in (e) and shows the presence of a cross-sectional intergranular crack within the CrN toplayer, which stops at the CrN-Cr interface. The arrows in (d) indicate the positions of glide planes passing through columnar ductile Cr crystallites, as visible also in Fig. 4b.

integrated radially and azimuthally in order to obtain a qualitative information on the occurrence of micro- and nanoscopic morphological and microstructural features within the X-ray beam gauge volume of $(x \times y \times z) = (20{,}000 \times 35 \times 50)$ nm^3. Fig. 6 shows small-angle X-ray scattering microscopy (SAXSM) micrographs compiled from the CSnanoXRD data collected from the two scratch cross-sections (Fig. 2).

In the SAXSM micrograph from the *200 mN scratch track* (Fig. 6a), the surface and the film-substrate interface can be clearly resolved due to their higher scattering contrast (Fig. 6a). Furthermore, the difference in the electron density between CrN and Cr and probably also in a higher concentration of structural defects within brittle nanoceramic CrN makes it possible to resolve the two sublayers. The latter is supported by findings from Ref. [40], as well as the as-deposited in-plane stress magnitudes $\sigma_{22}^{m}(y,z)$ presented in Suppl. Fig. 2 and discussed later in Sec. 3.5. A U-like distribution of significantly scattering intensity is however observed symmetrically within the near-surface CrN toplayer mainly (i) at distances of ~500 nm to ~3 μm from the imprint centre and (ii) close to the CrN-Cr interface in the imprint centre with a symmetrical lateral extent of ~3 μm (Fig. 6a). The increased SAXS intensity indicates an increased presence of micro- and nanoscopic morphological-microstructural changes or defects within the toplayer, which correlate well with particular $\sigma_{22}^{m}(y,z)$ concentrations discussed in detail in Sec. 3.5. At this stage, it can be supposed that the increased SAXS intensity is caused by a mutual sliding of V-shaped grains and formation of nanoscopic intergranular cracks like in Fig. 3a-c.

In the SAXSM micrograph from the *400 mN scratch track* (Fig. 6b), both sublayers, the surface and the substrate can be again clearly distinguished. Within the scratch track area, a significant rise in the SAXS intensity from the CrN toplayer indicates again higher densities of through-thickness intergranular cracks (cf. also Figs. 3d,e) and of nanoscopic intragranular defects formed as a result of CrN toplayer fragmentation (cf. Fig. 5c), as indirectly confirmed by the texture data in Fig. 5d, in agreement with the results from Wiecinsky et al. [16,18].

A comparison of the two SAXSM micrographs in Fig. 6 indicates also different degrees of the compression and pile-up formation of the particular Cr sublayers, both more pronounced in the 400 mN sample (Fig. 6b). Remarkably, SAXSM micrographs documents that the thickness of the CrN toplayers remains practically unchanged, irrespective

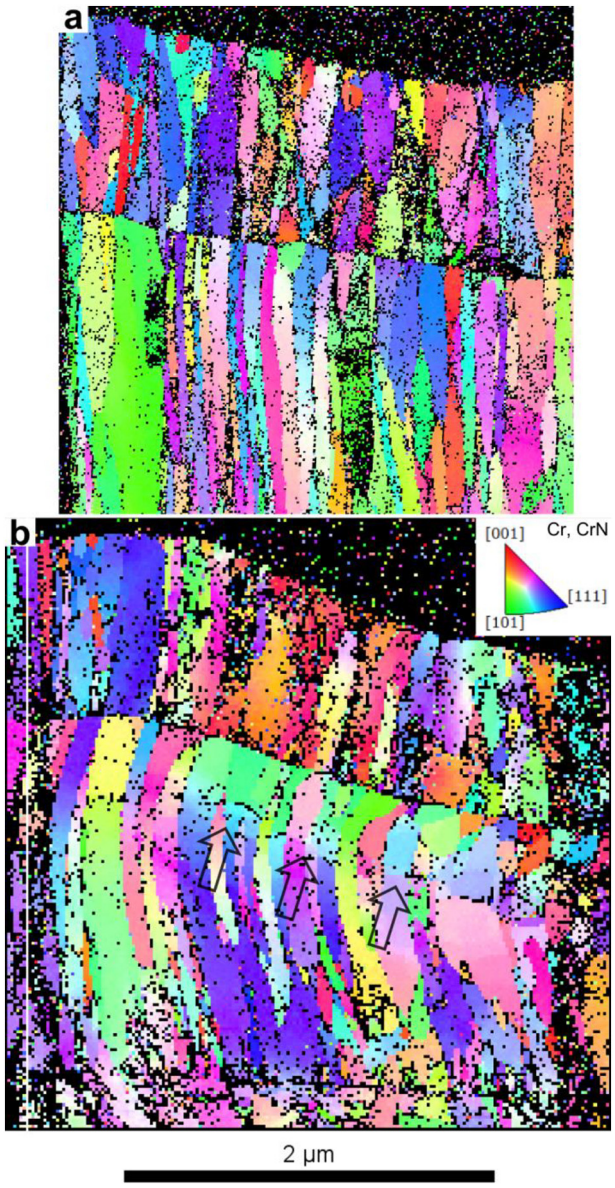

Fig. 4. TKD maps acquired from the respective TEM lamellae with the 200 mN (a) and 400 mN (b) scratches show orientations of columnar CrN and Cr crystallites with respect to the out-of-plane [001] film orientation. The arrows in (b) indicate scratch-induced changes in the crystallites' orientation caused by plastic deformation of the ductile Cr. The respective glide planes are visible also in Fig. 3d.

of the applied load magnitude. Furthermore, it should be noted, that the plastic deformation of the Cr sublayers (cf. Figs. 3-5) did not obviously lead to changes in SAXS intensities in Fig. 6, since deformation-induced dislocation movement does not affect the electron density in the investigated volume significantly.

3.3. 2D FWHM analysis

2D diffraction patterns collected in the CSnanoXRD experiments were integrated cake-like using azimuthal integration range of $\Delta\delta=$ 10 deg. over the whole DS rings' azimuthal range of $\delta = 0$–360 deg. in order to obtain 36 $I(\theta,\delta_i,y,z)$ dependencies. Afterwards CrN 111 and Cr 110 reflections were fitted using Gauss function and 36 FWHM (δ_i, y, z) were evaluated for every measurement position (y, z) as well as detector azimuthal position δ_i and then arithmetically averaged as $\mathrm{FWHM}(y,z)=\frac{1}{36}\sum_{i=1}^{36}\mathrm{FWHM}(\delta_i,y,z)$. Generally, the FWHM evaluated from DS rings is sensitive to the size of coherently diffracting domains, as well as to the presence of structural defects like dislocations, vacancies and other types of micro- and nanoscopic crystal lattice distortions, which can be denoted as *microstrains* of 2nd and 3rd order. Thus, by comparing the FWHM distributions from regions affected by scratch tests with regions of intrinsic defect density (formed during the deposition process, cf. Refs. [40, 51]), qualitative conclusions can be drawn on changes in size of coherently diffracting domains and/or microstrains as a result of the scratch process. In contrast to the SAXSM results from Fig. 6, FWHM data reflect only scratching-induced structural changes within the crystallites and are therefore insensitive to the presence of intergranular cracks and pores in the X-ray gauge volume.

Figs. 7 shows respective FWHM(y, z) of CrN 111 and Cr 110 reflections evaluated from the CSnanoXRD data. For the *200 mN scratch track*, a relatively homogenous FWHM increase can be observed in CrN toplayer within in the imprint centre with a symmetrical lateral extent of ~2 μm. In the Cr sublayer, the FWHM increase is localized at distances of ~4 μm from the imprint centre. For the *400 mN scratch track*, a significantly larger and homogenous increase in FWHM can be again observed within the CrN toplayer, whereas partially localized FWHM increase in Cr interlayer was detected at the positions of ~5 μm from the imprint centre as well as Cr-CrN interface.

The cross-sectional and lateral occurrence of the increased FWHM values in CrN and Cr sublayers (Fig. 7) correlate well with the changes of out-of-plane residual stress concentrations $\sigma_{33}^{m}(y,z)$ from Figs. 8b and 9b. In the CrN toplayers, the FWHM increase correlates with the build up a high compressive stresses $\sigma_{33}^{\mathrm{CrN}}(y,z)$, up to −2 GPa in the *400 mN scratch track* (Figs. 7b and 9b). In the Cr sublayer, the FWHM increase correlates with the build up a high tensile stresses $\sigma_{33}^{\mathrm{Cr}}(y,z)$ up to ~2 GPa (Figs. 7, 8b and 9b). Therefore, the FWHM increase in the CrN toplayers (Fig. 7) can be interpreted by (i) the compaction of the CrN toplayer due to the normal force induced by the sliding indenter, resulting in large out-of-plane compressive stress (cf. Sec. 3.5), (ii) the nanoscopic intragranular fracturing of CrN crystallites mainly due to the friction force oriented along the x-direction, (iii) gradients of 1st order strains within the gauge volume and (iv) the irreversible deformation of the CrN grains, as documented by bulged form of the CrN grains in Fig. 3e. Especially the gradual FWHM increase towards the surface in the CrN toplayer of the *400 mN scratch track* in Fig. 7b supports the concept of the near-surface fracturing induced by the friction mechanism. In the case of Cr interlayers, the symmetric and localized FWHM increases (Fig. 7) can be correlated with the bulging of Cr crystallites and their plastic deformation during the imprint formation. Note that in Fig. 7b, the FWHM increase in the Cr spans the whole width of the measured sample region.

The findings from Fig. 7 are complementary to the SAXSM-data from the CrN topalyers presented in Fig. 6. Whereas the localized SAXS intensity increase in both scratch imprints (Fig. 6) can be correlated with the intergranular cracks and pores formation in CrN mainly due to the changes in $\sigma_{22}^{\mathrm{CrN}}(y,z)$ magnitudes, the FWHM increase across the CrN sublayers documents an increase in the crystal defect density. This is mainly due to the imprint formation, which is accompanied by the CrN grain boundary sliding [caused by the normal force of the indenter (Figs. 8b and 9b), which also results in compressive $\sigma_{33}^{\mathrm{CrN}}(y,z)$ in the same region]. Furthermore there is also transgranular cracking (probably due to the friction force), which induces the reduction of the size of coherently diffracting domains and consequently the FWHM increase (cf. Fig. 3e).

3.4. Qualitative texture analysis

Qualitative texture analysis was carried out in order to study cross-sectional changes to the Cr and CrN crystallites' orientations due to

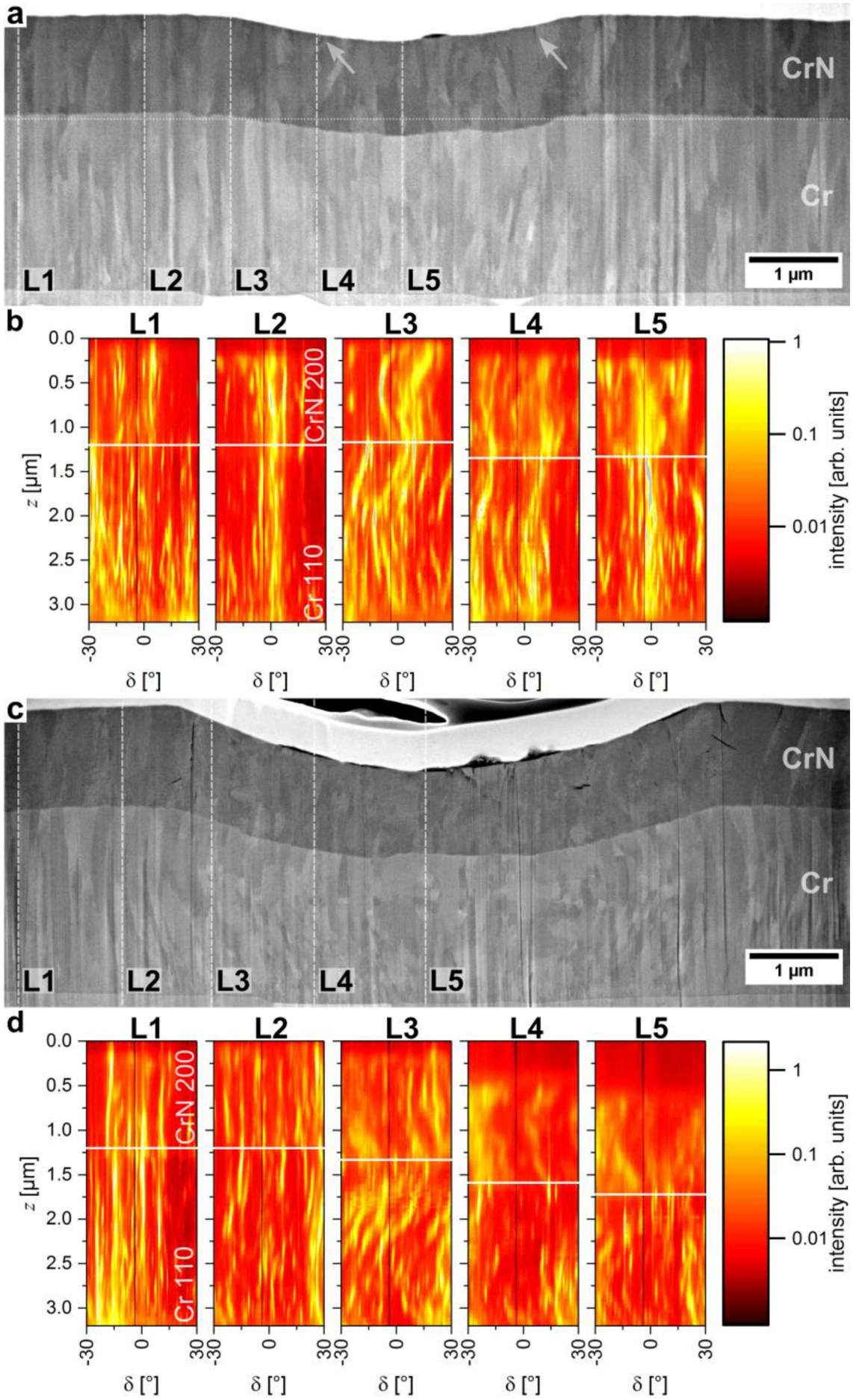
a
CrN
Cr
L1
L2
L3
L4
L5
1 µm
b
L1
L2
L3
L4
L5
CrN 200
Cr 110
z [µm]
δ [°]
intensity [arb. units]
c
CrN
Cr
L1
L2
L3
L4
L5
1 µm
d
L1
L2
L3
L4
L5
CrN 200
Cr 110
z [µm]
δ [°]
intensity [arb. units]

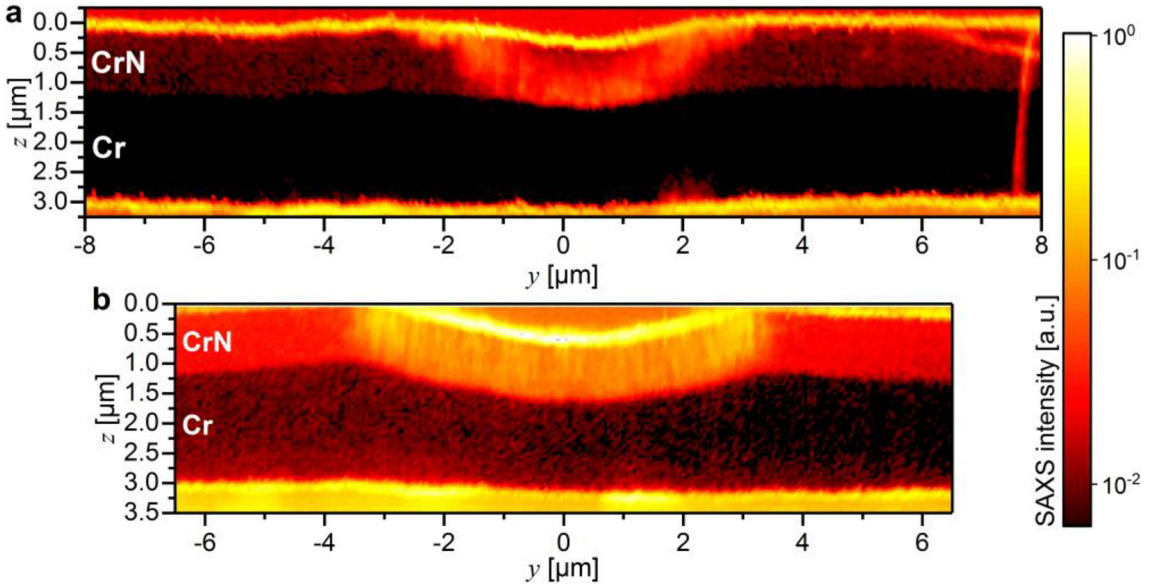

Fig. 6. Small angle X-ray scattering microscopy (SAXSM) micrographs evaluated from 32,421 and 26,361 2D diffraction patterns collected from the 200 mN (a) and 400 mN (b) scratches, respectively. Their high scattering contrast allows resolving the interfaces and sublayers within the Cr/CrN/HSS sample. The scratch performed with 400 mN induced a significant Cr interlayer thickness reduction and also the formation of symmetrical pile-ups (b). The U-like regions with increased SAXS intensities within the CrN toplayer were attributed to the formation of micro- and nanoscopic intergranular cracks, as documented in Fig. 3, and also to a reorientation of CrN crystallites, as documented by the texture data in Figs. 5b,d. In addition, the shape of these high-intensity regions correlates well with the decreased in-plane stress magnitude in Figs. 8a and 9a.

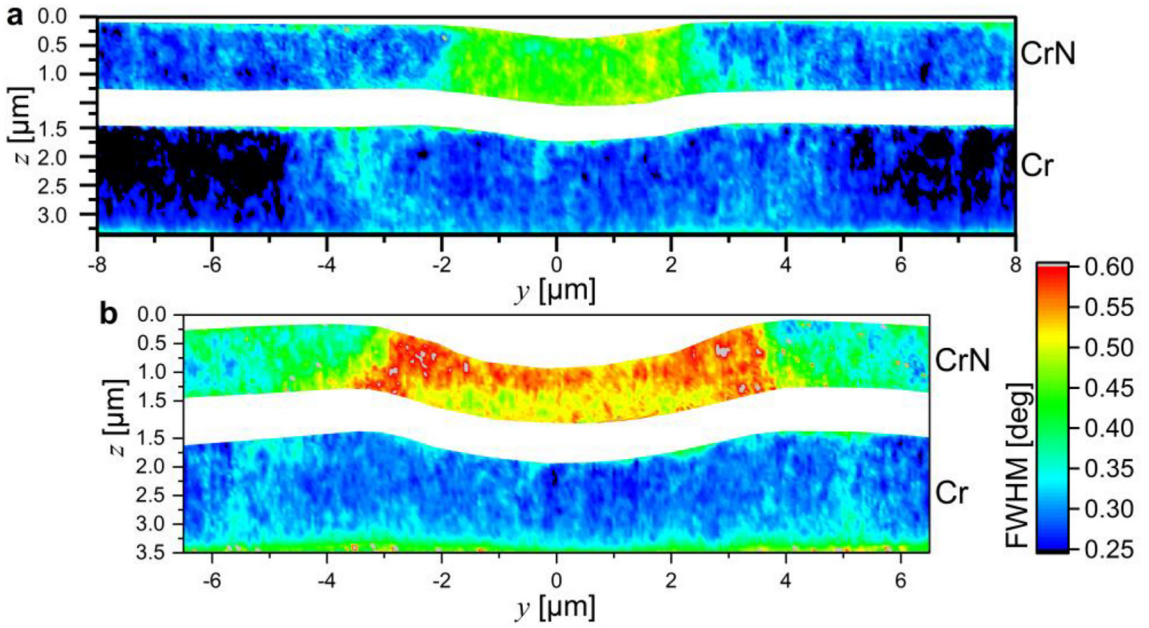

Fig. 7. FWHM micrographs evaluated from 32,421 and 26,361 2D diffraction patterns collected from the 200 mN (a) and 400 mN (b) scratches, respectively. The CrN 111 FWHM increase is caused by nanoscopic intragranular fracturing of CrN crystallites due to the large out-of-plane compressive stress imposed by the indenter during the scratching. The symmetric and localized Cr 110 FWHM increases can be correlated with a bending of Cr crystallites and their plastic deformation. The cross-sectional occurrence of the increased FWHMs in both materials correlate well with the changes of out-of-plane residual stresses $\sigma_{33}^{m}(y,z)$ from Figs. 8b and 9b.

Fig. 5. SEM micrographs (a) and (c) from FIB-fabricated cross-sections of the 200 and 400 mN scratch tracks, respectively, reveal the columnar grained microstructure and tilting/ bending of the needle-like crystallites up to ~15 and ~ 25 deg. with respect to the film surface normal direction. In the CrN toplayer, dark regions indicate the presence of cracks, which are seen to propagate in (c), across the whole toplayer at the locations of the pile-ups. Respective DS ring azimuthal intensity plots $I(\delta,z)$ in (b) and (d) were evaluated from CSnanoXRD data collected along the dashed lines L1-L5 in (a) and (c), respectively. CrN 200 $I(\delta,z)$ plots from predominantly ⟨100⟩ fibre textured crystallites show smearing of vertical intensity lines and indicate thus incrementing fragmentation the brittle CrN towards the imprint centres, as supported also by SAXSM data in Fig. 6. Cr 110 $I(\delta,z)$ plots indicate a ⟨110⟩ fibre texture, whereas the oscillatory vertical intensity lines document the tilting of the Cr columnar crystallites caused by the plastic deformation present in this layer.

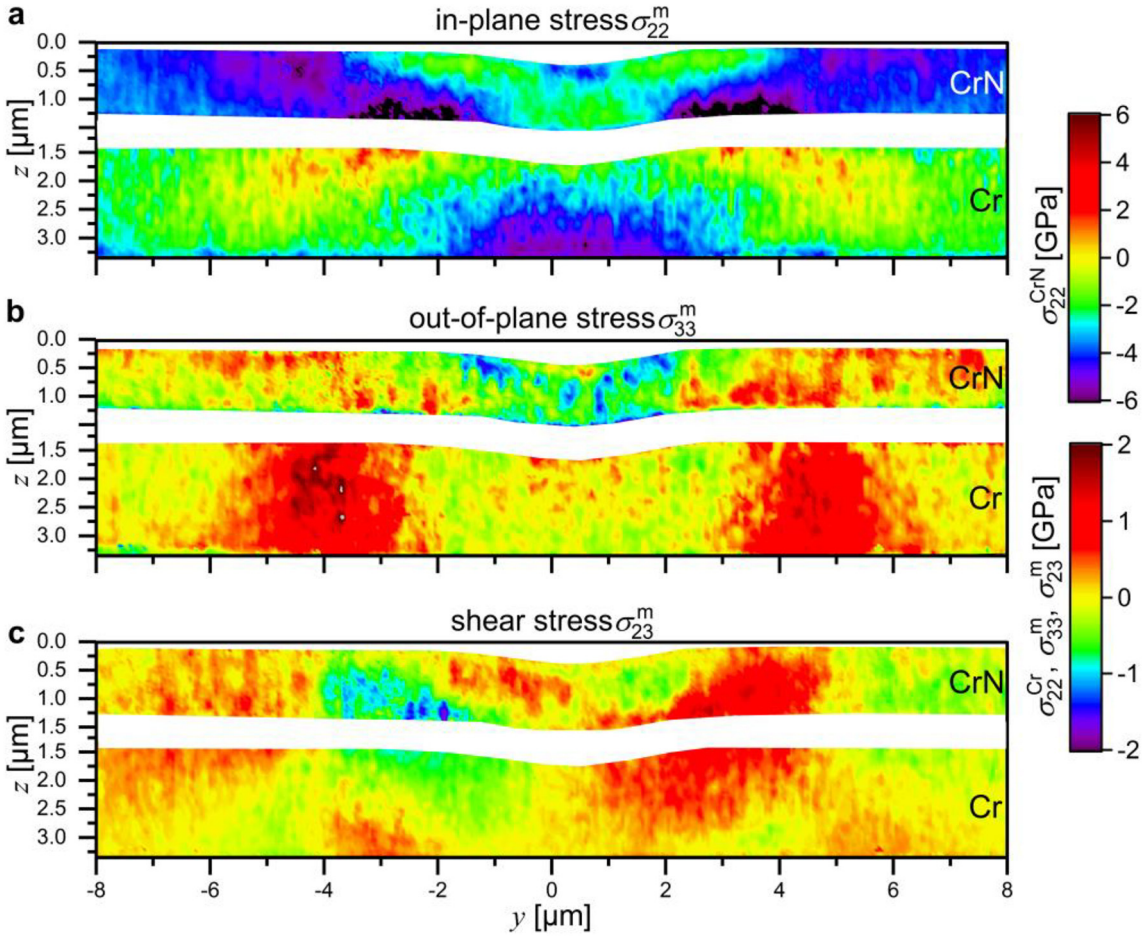

Fig. 8. Experimental in-plane $\sigma_{22}^{m}(y,z)$ (a), out-of-plane $\sigma_{33}^{m}(y,z)$ (b), and shear $\sigma_{23}^{m}(y,z)$ (c) stress distributions evaluated from the cross-section of the 200 mN scratch track area. Note that $\sigma_{22}^{CrN}(y,z)$ is displayed with a different stress scale. The data were evaluated from 32,421 2D diffraction patterns.

scratching. For this purpose, azimuthal intensity distributions of CrN 200 and Cr 110 DS rings were evaluated from CSnanoXRD data collected along the dashed vertical lines indicated in Figs. 5a and c. Due to the small CSnanoXRD probe size, the diffraction statistics were rather limited, but still allowed to evaluate texture changes qualitatively. The logarithmic plots in Figs. 5b and d show azimuthal DS rings diffraction intensities from a selected azimuthal δ angle range of ± 30 deg., with respect to the $\delta = 0$ deg. diffraction vector orientation, which corresponds approximately to the film normal direction (cf. Fig. 1, Fig. 5b,d). The distinct vertical intensity lines in Figs. 5b,d represent diffraction intensities from fibre-textured crystallites with approximately identical orientations with respect to the sample normal. Therefore, the azimuthal positions of the lines can be used to determine the relative orientation of crystallites with respect to the sample surface normal.

The straight vertical intensity lines within plots L1 and L2 of Figs. 5b and plot L1 of Fig. 5d indicate the presence of crystallites with orientations unaffected by scratching, where CrN 200 DS ring azimuthal maximum was observed at 0 deg. down to a depth of ~1.2 µm, which allows us to identify a ⟨100⟩ fibre texture. In the deeper regions of the bilayer film, at depths of ~1.2–3.2 µm, the presence of a ⟨110⟩ fibre texture can be deduced in Cr (Fig. 5b,d), in good agreement with Refs. [19, 20, 40]. The plots L3 and L4 with curved intensity lines in Fig. 5b indicate a bending of crystallites within both sublayers, in agreement with the SEM micrograph in Fig. 5a. The plot L5 from the scratch track centre with straight but much broadened intensity lines indicates a fibre texture blunting and weakening of preferred crystallite orientation in both sublayers within the 200 mN scratch track cross-section (Fig. 5b). Similar, also the plots L2-L5 in Fig. 5d from the 400 mN scratch track cross-section show intensity lines shifted up to an angle of ~25 deg. counter-clockwise and a steadily increased broadening of the lines towards the scratch track centre, consistent with Ref. [52], indicating a heavy deformation of the grain microstructure, especially in CrN.

There is, however, a striking difference between the DS azimuthal distributions obtained from the CrN brittle and Cr ductile sublayers in Figs. 5b and d. A predominant smearing of the intensity lines collected from the deformed CrN toplayers indicates fracturing of the nanoceramic nitride beneath the scratch track, which results in a large orientation spread and fibre texture blunting. The CrN toplayer fracturing correlates well with the increased SAXS and FWHM intensities in Figs. 6 and 7 and also with decreased in-plane $\sigma_{22}^{m}(y,z)$ and increased out-of-plane $\sigma_{33}^{m}(y,z)$ stress magnitudes, respectively, presented in Sec. 3.5. In the case of Cr sublayers, however, predominantly oscillatory cross-sectional profiles of the intensity lines and less pronounced smearing (Fig. 5b,d) suggest that the irreversible deformation of the metallic ductile Cr sublayers was accommodated by bending/bulging and plastic deformation of the columnar grains, in agreement with the electron microscopy data from Figs. 3 and 4 and partly also with the FWHM data from Fig. 7.

3.5. Stress analysis across scratch track cross-sections

Ex-situ analysis of residual stress distributions was carried out using the methodology described by Ref. [33] and depicted in the Supplementary Material. At first, residual stress gradients $\sigma_{22}^{Cr}(z)$ and $\sigma_{22}^{CrN}(z)$ across

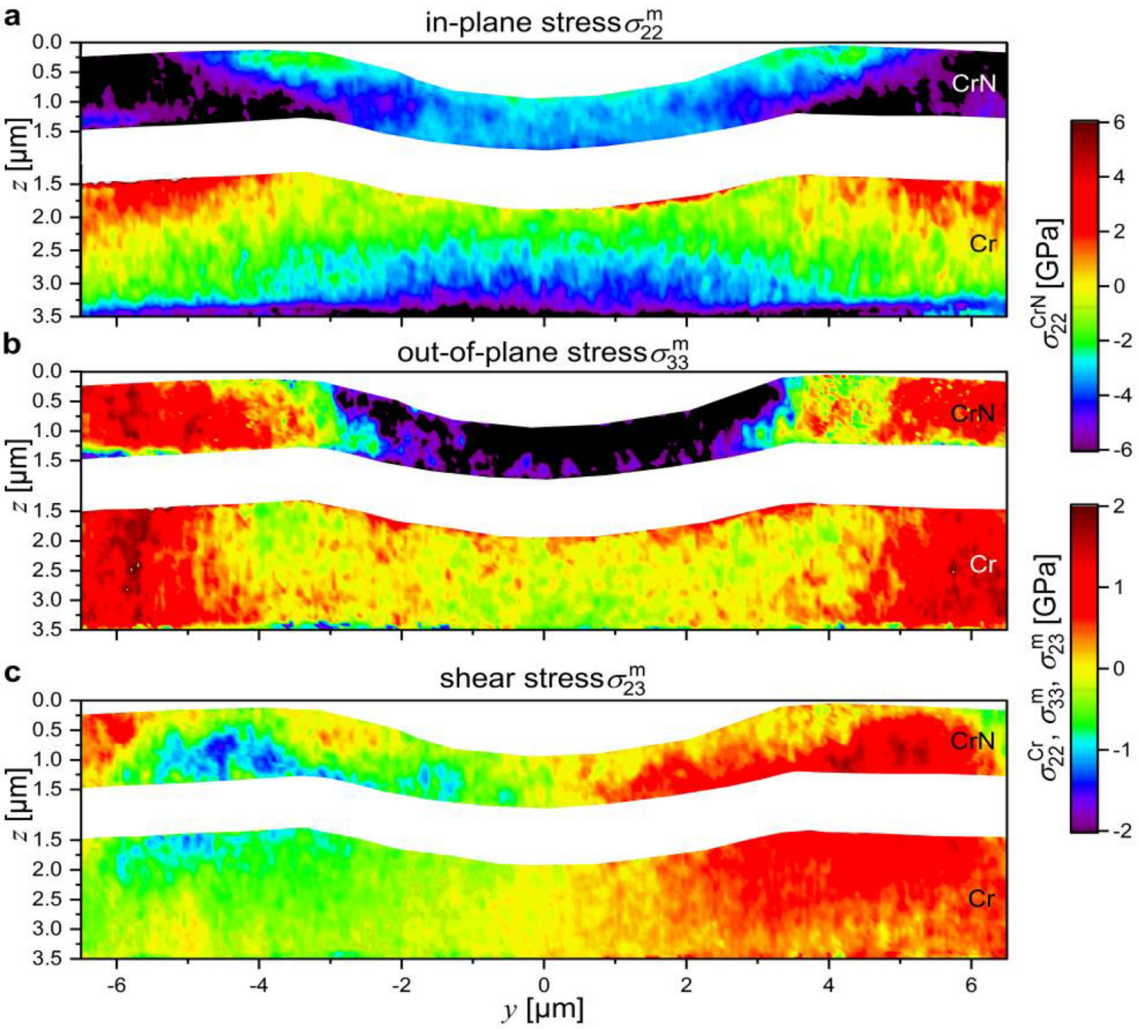

Fig. 9. Experimental in-plane $\sigma_{22}^m(y,z)$ (a), out-of-plane $\sigma_{33}^m(y,z)$ (b), and shear $\sigma_{23}^m(y,z)$ (c) stress distributions evaluated from the cross-section of the 400 mN scratch track area. Note that $\sigma_{22}^{CrN}(y,z)$ is displayed with a different stress scale. The data were evaluated from 26,361 2D diffraction patterns.

the Cr and CrN sublayers were determined using Eq. 4 from a CSnanoXRD line scan collected far off the scratch tracks, where the material was unaffected by the scratch experiment. As indicated in Suppl. Fig. 2, the stress magnitude in the Cr interlayer is nearly constant at ~-1 GPa, whereas the compressive stresses in CrN increases from −3 GPa at the CrN-Cr interface to −4 GPa at the surface. The compressive stresses in Cr and CrN in the as-deposited film can be attributed to ion-bombardment during film growth and additional thermal stress formed during cooling down from the deposition temperature, as extensively discussed in Refs. [40, 51].

3.5.1. Cross-sectional 2D stress distributions for the 200 mN scratch

Cross-sectional residual stress distributions consisting of in-plane $\sigma_{22}^m(y,z)$, out-of-plane $\sigma_{33}^m(y,z)$ and shear stress $\sigma_{23}^m(y,z)$ magnitudes across the 200 mN scratch track area are presented in Fig. 8. The results document complex lateral and depth gradients of the stresses, which are a result of the intrinsic stress state developed in the film during deposition (Suppl. Fig. 2) and the scratch-induced residual deformation of the bilayer (Fig. 8). The latter includes (i) a bending of the CrN toplayer under the indenter tip, similar to the bending of a clamped cantilever, accompanied by a thickness reduction of the Cr sublayer due to plastic flow (Fig. 2) and (ii) a subsequent partial film curvature relaxation after the indenter tip had translated to further positions on the specimen's surface [26,53,54].

This bending-like deformation of the CrN toplayer results (i) in the formation of in-plane tensile stresses at the virtual clamping positions outside the deformed zone and compressive in-plane stresses in the centre of the deformed zone in the CrN near-surface region and (ii) in the formation of alike stress distributions of opposite signs at the CrN-Cr interface. When the fracture stress of CrN is locally exceeded within the tensile stressed zones, nanoscopic cracks are formed within the CrN toplayer (Fig. 3b,c), which results in a relaxation of stresses and subsequently in the formation of compressive stresses during elastic rebound after the indenter tip has moved away.

Within the CrN toplayer, this results in the observed decrease of the relatively high compressive stresses of ~ −4 GPa (in the as-deposited state) to ~ −1 GPa within (i) the near-surface region at distances of ~500 nm to ~4 µm from the imprint centre and (ii) at the CrN-Cr interface directly under the imprint centre with a symmetric lateral extent of ~3 µm (Fig. 8a). Furthermore, the preservation of the compressive stress at the surface of the imprint centre and the accumulation of even higher compressive stresses up to −6 GPa at the CrN-Cr interface at distances of 2 µm to 5 µm left and right of the imprint centre can also be related to this bending-like deformation (Fig. 8a). Additionally, the compressive stress increase found at distances of 5–7 µm from the centre at the sample surface (outside the virtual clamping positions) is related to the aforementioned elastic rebound after passing of the scratching indenter. The occurrence and the U-shape of the CrN sublayer regions, where the

relaxed $\sigma_{22}^{CrN}(y,z)$ compressive stresses are present in Fig. 8a, correlate well with the SAXSM data from Fig. 6a and confirm the assumption that the relaxation was accompanied by intergranular grain boundary sliding and intergranular cracking in CrN (Fig. 3a-c), which stops within the CrN toplayer (cf. Secs. 3.1 and 3.2).

Within the Cr sublayer, the in-plane stress distribution $\sigma_{22}^{Cr}(y,z)$ exhibits relatively high compressive stresses with a magnitude of ~ −1.8 GPa directly at the imprint centre (Fig. 8a). These originate from the process of (i) the sublayer compression and plastic deformation during loading and (ii) subsequent sublayer curvature relaxation resulting in elastic contraction in the Cr imprint centre, after the indenter tip had moved to further sample position, in agreement with Refs. [26, 53, 54]. Additionally, there are symmetric tensile stress regions $\sigma_{22}^{Cr}(y,z)$ with up to 800 MPa magnitude located directly next to regions with the highest compressive stress magnitude in CrN (Fig. 8a). These tensile stress concentrations in the Cr sublayer can be attributed to the bending of the CrN toplayer during the scratch experiment leading to an elongation of the Cr sublayer, whose further relaxation after scratching was however hindered by the deformed CrN toplayer. The corresponding stress fields $\sigma_{22}^{Cr}(y,z)$ are similar to those resulting from foreign object damage, as reported for a hard steel sphere impacting on a Ti alloy in Refs. [55, 56], indicating similar deformation mechanisms as during high-rate loading of a ductile material. Furthermore, the reduction and increase of in-plane compressive stress $\sigma_{22}^{m}(y,z)$ in CrN and Cr, respectively, directly under the scratch track groove, is in particular agreement to findings from Khan et al. [23], where scratching of an Al-alloy also led to formation of tensile and compressive stresses in surface-near and sub-surface regions, respectively, directly under the scratch track groove.

For the $\sigma_{33}^{CrN}(y,z)$ distributions in Fig. 8b, minor compressive stresses in the range of ~ −500 MPa were revealed around the residual imprint centre over the CrN toplayer thickness with a lateral extent of ~4 μm. These are a consequence of the deformation-induced compaction of the toplayer by the sliding indenter and the remaining residual deformation. The central region is symmetrically surrounded by tensile stressed areas with a magnitude of ~800 MPa. These tensile stresses revealed besides the scratch track, starting 2 μm away from the centre at the CrN-Cr interface and extending over 4 μm at the Cr-HSS interface, can be attributed to the curvature relaxation after the further movement of the indenter. The same $\sigma_{33}^{Cr}(y,z)$ stress behaviour is observed in the Cr sublayer, where the tensile stress reaches a maximum of ~1.8 GPa (Fig. 8b). Generally, the out-of-plane stresses must represent continuity across the CrN-Cr interface, which is not the case within the contact zone of the sliding indenter. This discontinuity is most probably related to a a_0^{CrN} decrease within the process zone, as a consequence of compaction of the (partly) fragmented CrN crystallites (cf. Figs. 3a-c, 6a and 7a), which expresses as a virtual out-of-plane compressive stress.

Compressive out-of-plane stresses directly under the indenter tip are well accounted for during in-situ CSnanoXRD experiments on thin films [33,34], however, they were not found during prior synchrotron X-ray experiments carried out on scratched Al-Alloys [23], which can be attributed to much higher stress relief through plastic deformation of the Al-alloys during scratching.

The development of the shear stress $\sigma_{23}^{m}(y,z)$ is also dominated by the bending-like deformation and is antisymmetric with respect to the y-axis (Fig. 8c). The shear stresses are (in this case) a y-axis coordinate-dependent representation of the change of the principal stress orientation, which means positive shear stress in the positive y-axis half represents coordinate-dependent positive (counter-clockwise) rotation of the principal stress tensor, whereas negative shear stress in the negative y-axis half of the stress field represents the opposite, i.e. clockwise rotation (Fig. 8c). Concerning the CrN toplayer, the shear stress distribution reflects the mainly bending-like deformation, whereas in the Cr the distribution of shear stress represents the more complex stress state of $\sigma_{22}^{Cr}(y,z)$ from Fig. 8a.

3.5.2. Cross-sectional 2D stress distributions for the 400 mN scratch

After scratching the thin film with 400 mN load, the scratch groove exhibits significantly larger curvature compared to that of the 200 mN scratch (Figs. 2, 5a,c, 6). The scratch test resulted in bending of the CrN toplayer, compaction of the Cr interlayer and in the formation of symmetric pile-ups (Figs. 2b, 5c, 6b). Consequently, the $\sigma_{22}^{m}(y,z)$, $\sigma_{33}^{m}(y,z)$ and $\sigma_{23}^{m}(y,z)$ distributions shown in Fig. 9 exhibit relatively high stress concentrations and reflect crack formation within the sublayers.

Fig. 9a indicates that the bending-like of the CrN toplayer resulted in the relaxation of compressive in-plane stress $\sigma_{22}^{CrN}(y,z)$ mainly beneath the scratch track groove, as described in detail in Section 3.5.1. This relaxation can be attributed to the formation of cracks, as visible in Fig. 3d and 5c and due to the deformation-induced localized tensile stress build-up, the magnitude of which exceeded the fracture strength of brittle CrN. An additional contribution is given by the friction-induced tension of the film along the x-direction, which also results in tensile stress build-up and cracking [26,54,57]. Next to the scratch groove, however, high compressive in-plane stresses $\sigma_{22}^{CrN}(y,z)$ in CrN up to −6 GPa are revealed. These are a consequence of the symmetric pile-up formation, the CrN toplayer elongation and its subsequent elastic contraction, which was however hindered by the underlying Cr. The nearly complete relaxation of the compressive stresses $\sigma_{22}^{CrN}(y,z)$ within the U-shaped groove (Fig. 9a) correlates well with SAXSM (Sec. 3.2), FWHM (Sec. 3.3) and texture (Sec. 3.4) data and supports the suggested assumption of intergranular cracking (Fig. 3e) and intragranular fragmentation of the brittle CrN (Secs. 3.3 and 3.4).

The in-plane stress distribution $\sigma_{22}^{Cr}(y,z)$ in the Cr-sublayer (Fig. 9a) is qualitatively similar to that developed after scratching at the load of 200 mN (Fig. 8a), with a comparatively higher lateral extent of the compressively stressed areas and a remarkable compressive-to-tensile stress gradient across the sublayer. As already discussed above, the compressive stresses $\sigma_{22}^{Cr}(y,z)$ within the Cr-sublayer next to the HSS interface originate from the elastic contraction of the elongated sublayer after the scratch experiment. Since this elastic contraction was hindered by the CrN toplayer next to the CrN-Cr interface, tensile stresses were formed in the upper regions of the Cr sublayer (Fig. 9a). The higher stresses in the 400 mN sample are similar to impact test in Refs. [55, 56], where a higher lateral extent of the stress fields and more pronounced pile-up formation due to foreign object damage was found when using a higher impact speed. Again, the reduction and increase of in-plane compressive stress $\sigma_{22}^{m}(y,z)$ in CrN and in Cr, respectively, directly under the residual imprint of the indenter, is in agreement to findings from Khan et al. [23], cf. Sec. 3.5.1.

The out-of-plane stress distribution $\sigma_{33}^{CrN}(y,z)$ in Fig. 9b shows high compressive stress magnitudes up to −2 GPa within the scratch groove, which can be correlated with irreversible microstructural changes within the CrN sublayer (cf. Sec. 3.1.-3.4) and the pronounced surface curvature, which hindered surface relaxation after scratching. Besides the scratch track only minor tensile stresses were revealed in Fig. 9b. In the Cr-sublayer, qualitatively the same stress distribution $\sigma_{33}^{Cr}(y,z)$ is visible as for the scratch carried out with 200 mN load, with a higher lateral extent of the stress-free zone in the centre of the scratch track groove. Again, the discontinuity of $\sigma_{33}^{m}(y,z)$ across the CrN-Cr interface found within the contact zone of the sliding indenter could be related to unstressed lattice parameter changes, as explained in Section 3.5.1 and documented by Figs. 3e, 6b and 7b.

Relatively modest shear stress distributions $\sigma_{23}^{m}(y,z)$ (Fig. 9c) revealed in both layers beneath the scratch track (y-positions from −3 to 3 μm) document the uniaxial compaction of the CrN grains after cracking along the columnar grain boundaries and the dominance of in-plane stresses after the plastic deformation in the Cr sublayer. Besides the scratch track, there is a relaxation-induced local rotation of the principal stress axes, which is indicated by the accumulation of interface-near shear stresses with a magnitude up to −1.5 GPa at y-positions from −6 to −4 μm and with a magnitude up to 1.5 GPa at y-positions from 4 to 6 μm (Fig. 9c).

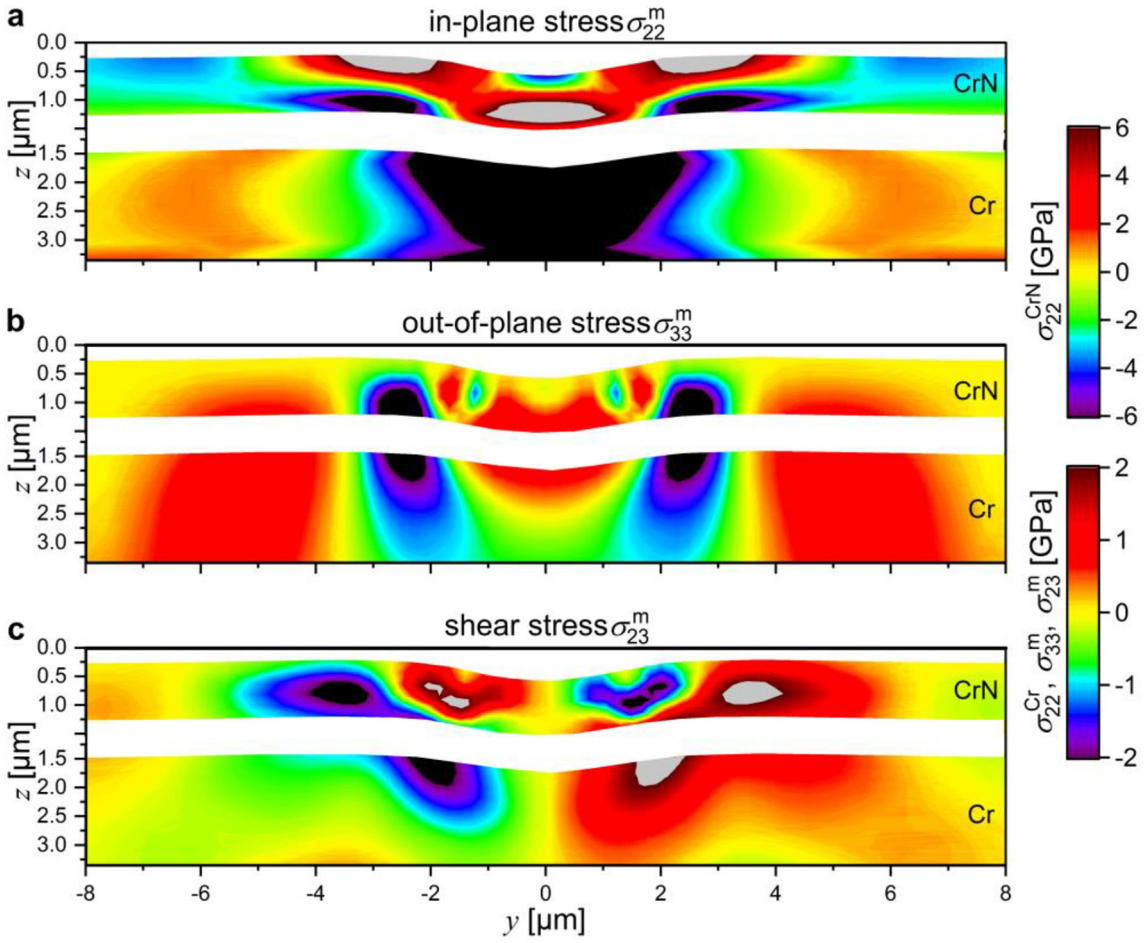

Fig. 10. FEM calculated in-plane $\sigma_{22}^{m}(y,z)$ (a), out-of-plane $\sigma_{33}^{m}(y,z)$ (b), and shear $\sigma_{23}^{m}(y,z)$ (c) stress distributions evaluated for the cross-section in the centre of the 200 mN scratch track. Note that $\sigma_{22}^{CrN}(y,z)$ is displayed with a different stress scale.

3.6. Finite element model

In order to describe the deformation processes during the scratch experiments and to interpret the experimental stress distributions $\sigma_{ij}^{m}(y,z)$ in CrN and Cr, a 3D FE model was implemented. The calculated stress distributions for the scratch tracks performed with 200 and 400 mN load are displayed in Figs. 10 and 11.

3.6.1. Modelled stress distributions for the 200 mN scratch track

The calculated stress distributions $\sigma_{ij}^{m}(y,z)$ across the 200 mN scratch track area are displayed in Fig. 10. High tensile stress concentrations $\sigma_{22}^{CrN}(y,z)$ are found symmetrically in the CrN toplayer at lateral distances of 2 to 4 µm at the surface, as well as in the centre of the groove at the Cr/CrN interface with a lateral extent of 2 µm (Fig. 10a). Additionally, high compressive stress $\sigma_{22}^{CrN}(y,z)$ with a magnitude of −6 GPa is found at the respectively opposing sides of the CrN layer (Fig. 10a). Additionally, at distances larger than 5 µm from the imprint centre, compressive stresses $\sigma_{22}^{CrN}(y,z)$ can be found in the CrN toplayer.

While the magnitude of compressive stress $\sigma_{22}^{CrN}(y,z)$ found in the experiment is particularly well reflected by the model (cf. Figs. 8a), tensile stress magnitudes found in the model are exaggerated compared to the experimental data. This is a consequence of stress-relief due to nanoscopic crack formation in the tensile stressed zones formed during the experiment (cf. Figs. 3a–c, 5a, 6a) and possible grain boundary sliding in the centre of the scratch track, which are both unaccounted for by the model. In the Cr sublayer, in-plane stress $\sigma_{22}^{Cr}(y,z)$ magnitudes below −2 GPa were found in the imprint centre by the 3D FE model, which were symmetrically surrounded by regions of tensile stress (y outside ±4 µm), in a good agreement with the experimental data.

The symmetric out-of-plane tensile stress concentrations $\sigma_{33}^{CrN}(y,z)$ and $\sigma_{33}^{Cr}(y,z)$ in Fig. 10b outside the scratch track agree particularly well with the experimental results shown in Fig. 8b. A highly compressively stressed zone at distances of ~2 to 3 µm from the centre followed by a tensile stressed zone beneath the scratch track is however not validated by the experiment (Fig. 8b), which again is a consequence of the above-mentioned discrepancies between model and experiment (Fig. 3a,b). The out-of-plane stresses introduced through the scratch process have to be self-compensating, consequently, the stress-relief found in the experiment due to nanoscopic cracking leads also to a reduction of compressive stresses in the surrounding areas. The shear stress distribution $\sigma_{23}^{CrN}(y,z)$ obtained by the FE model is antisymmetric along the y-axis and reflects the bending-like deformation of the scratched area (Fig. 10c). The shear stress $\sigma_{23}^{Cr}(y,z)$ calculated for the Cr sublayer reflects the complex deformation beneath the scratch track groove and, similar to compressive in-plane stresses, fits very well to the experimental findings.

3.6.2. Modelled stress distributions for the 400 mN scratch track

In order to model the stress distributions $\sigma_{ij}^{m}(y,z)$ across the 400 mN scratch track area, cracks were introduced symmetrically at the edges of the groove (Fig. 11). Adding these two symmetric cracks accomplishes the aim to model the experimental stress distributions as accurately as

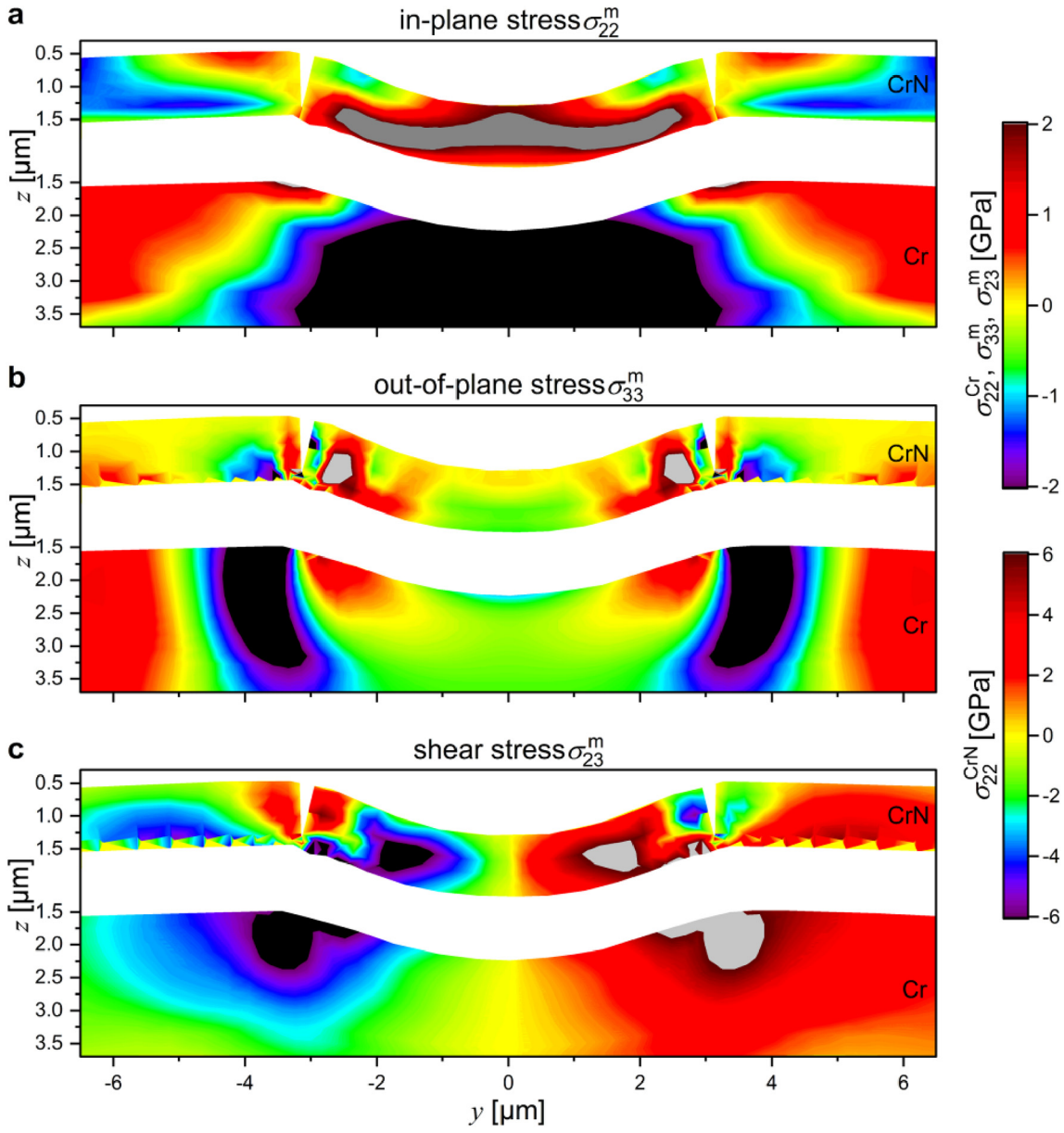

Fig. 11. FEM calculated in-plane $\sigma_{22}^{m}(y,z)$ (a), out-of-plane $\sigma_{33}^{m}(y,z)$ (b), and shear $\sigma_{23}^{m}(y,z)$ (c) stress distributions evaluated for the cross-section in the centre of the 200 mN scratch track. Note that $\sigma_{22}^{CrN}(y,z)$ is displayed with a different stress scale.

possible, while still maintaining the necessary computational time at a reasonable level. The observed relatively large differences between the experimental and modelled stress distributions $\sigma_{ij}^{m}(y,z)$ (cf. Figs. 9 and 11), however, can be explained by the formation of crack patterns and CrN fragmentation, as revealed by electron microscopy in Figs. 3e and 5c, as well as in the SAXS micrograph in Fig. 6b.

The calculated in-plane stress distributions $\sigma_{22}^{m}(y,z)$ for the CrN and Cr layers are shown in Fig. 11a. In the CrN toplayer, the stress distributions can be divided into two parts. First, within the residual imprint (y inside ± 3 µm), high tensile stress concentrations were revealed by the FE analysis, while besides the groove compressive stress was found. Comparing with the experimental data, the compressive stresses outside the scratch track groove are reproduced by the FE model (cf. Figs. 9a and 11a), but the modelled high tensile stresses within the residual imprint are not seen in the experimental results. This mismatch between the experimental and calculated data (Figs. 9a and 11a) can be interpreted by the above-mentioned computational restrictions and the massive microstructural changes in the CrN layer (cf. Figs. 3c-e, 4b, 5c), which resulted in $\sigma_{22}^{CrN}(y,z)$ stress relaxation within the scratch track area. In the Cr sublayer, high compressive stresses $\sigma_{22}^{Cr}(y,z)$ are found within the deformed zone, which is surrounded by tensile stressed regions, both in the experimental and the modelled data (Figs. 9a and 11a), as a consequence of the compression due to the sliding indenter and the pile-up formation, respectively. Concerning the out-of-plane stress $\sigma_{33}^{m}(y,z)$ (Fig. 11b) and shear stress $\sigma_{23}^{m}(y,z)$ (Fig. 11c) distributions, the calculated stresses in the Cr sublayer agree well with the experiment (Fig. 9b and c), whereas in the CrN toplayer the abovementioned difficulties regarding the FE model have to be considered.

In summary, Figs. 2-8 and 10 document the nanoscopic mechanical and microstructural response of a CrN-Cr bilayer thin film to scratch testing at two different loads. The elastic-plastic 3D-FE model allowed to assess the stress distributions in a satisfactory way, especially in the case of the 200 mN scratch (Fig. 10). In the case of 400 mN scratch, however, it was more challenging to properly model (Fig. 11) the multiaxial stress distributions from Fig. 9, because of the complex microstructural

changes especially in the CrN toplayer, like the high density of microcracks (Figs. 3e and 6b), which altered the mechanical response of the bilayer significantly.

4. Discussion of brittle-ductile CrN-Cr bilayer deformation

Mechanical failure of thin films during scratching experiments is influenced by a variety extrinsic and intrinsic factors [3–6,58]. In the case of nanocrystalline hard films, the particular microstructural and interfacial defects effectively responsible for failure are usually unknown. Similarly, complex stress concentrations around and behind the moving indenter tip, accompanying elastic and plastic deformation, chipping, cracking and delamination have remained unexplored experimentally [24].

Generally, the stress distributions accompanying failure are a superposition of elastic-plastic indentation stresses, frictional stresses and the residual internal stresses present in the film after the deposition [24,26,53,54]. The present work introduces a thorough ex-situ analysis of the residual stress gradients formed after the deposition (Suppl. Fig. 2) and multiaxial residual stress fields developed after the scratch experiment (Figs. 8,10). The experimental data and the FEM calculated stresses (Figs. 8-11) provide an accurate picture of the stress build-up after the two scratch tests, before the onset of critical failure, and also allow us to deduce the stress states under the indenter during the experiments.

According to prior investigation of the mechanical behaviour of CrN-Cr multilayer systems subjected to indentation, CrN can bear very high stress magnitudes up to −10 GPa in compression [17,34]. However, in tension, free-standing FIB-fabricated cantilever beams of magnetron sputtered CrN showed overall brittle fracture upon a (tensile) stress magnitude of ~5.8 GPa [45]. Consequently, it is reasonable to assume that high tensile and compressive stresses with CrN toplayers will be accommodated by the formation of inter- and intra-granular cracks within the nanoceramics, respectively. In the case of magnetron sputtered Cr thin films, compressive and tensile stress magnitudes are limited to ~3 GPa due to the onset of plastic deformation at higher stress levels [17,45].

Following, Figs. 8a and 9a document that complementary compressive and tensile in-plane stress build-ups are formed in the regions bordering the CrN-Cr interface, as a result of curvature relaxation after the scratching indenter tip had passed. This implicates that during the indenter loading, tensile stresses were formed at both sides of the CrN-Cr interface as a product of the large curvature (bending-like), whose formation, however, did not result in catastrophic failure of the bilayer. Importantly, the nanoscale stress distributions are correlated with morphological and microstructural changes within the brittle and ductile sublayers (Fig. 2-5). Therefore, it is possible to associate the above-implicated tensile in-plane stress formation in the brittle CrN toplayer with the formation of nanoscopic intergranular cracks (Fig. 3e) and intragranular defects (Figs. 6 and 7) as well as with the development of bilayer curvature. Similarly, the thickness reduction and pile-up formation within the ductile Cr (Fig. 2) is accompanied by a variety of microstructural changes like columnar grain bending and localized plastic deformation (Figs. 3-7).

Even though the STEM and SEM micrographs in Figs. 3e and 5c document the presence of cross-sectional cracks within the CrN toplayer, the underlying ductile Cr sublayer serves as an effective crack barrier. In other words, even though the fracture strength of CrN was exceeded in multiple places during the scratch test (Figs. 3,5), intergranular fracture along CrN columnar grains was arrested at the ductile Cr sublayer.

Similar to our previous study on the indentation behaviour of multilayered CrN/Cr films [17], also in the present case the ductile sublayers serve as an important stabilizing component to the bilayer's mechanical integrity during and after scratching. Their ability for thickness reduction, massive plastic deformation, crystallite bending and formation of pile-ups protects the brittle-ductile bilayer from critical failure at loads that would disintegrate a comparable monolithic CrN layer.

5. Conclusions

Cross-sectional X-ray nanodiffraction was used to assess multiaxial stress distributions and microstructural changes within a scratch-tested bilayer thin film at a resolution of 50 nm. The experimental results, encompassing also small-angle X-ray scattering micrographs that document nanoscopic microstructural changes, were correlated with electron microscopy analyses and a 3D finite element model. The quantitative results uncover the multiaxial residual stress build-up, which was clearly correlated to the nanoscopic deformation mechanisms within the brittle CrN and ductile Cr layers. While scratch testing results in intergranular grain sliding and intragranular grain fragmentation within the CrN nanoceramic toplayer, without any thickness reduction, the thickness reduction/extension of the ductile Cr interlayer is accompanied by transgranular plastic deformation with unidirectional gliding, formation of piles-up, as well as crystallite bending and rotation. The results confirm the beneficial influence of compressive residual stresses and the concept of ductile interlayers to stabilize the brittle components of thin films, especially by revealing the actual stress levels present at different loads in the respective individual layers. Several shortfalls of existing numerical analyses could thus be identified, in particular the failure to address the intergranular crack formation that originates from high tensile stresses in the brittle layer. In short, even though significant damage could be detected in the upper brittle CrN layer at higher scratch loads, the lower ductile Cr layer was able to absorb large amounts of deformation and continued to provide good adhesion, thus maintaining the functionality of the overall structure as a wear-resistant film.

Author Contributions Statement

M.M., J.K. and J.T. designed the project. M.M. performed the CSnanoXRD experiment and analysis, SEM, TKD and FIB analyses. J.Z. prepared the TEM samples and performed TEM analysis. W.E. performed the FE-simulation. M.R., S.N. and P.G. provided technical support and assistance as well as developed the MLLs optics setup at the ID13 beamline, ESRF. H.H., C.M., R.D. and W.E. contributed to the data interpretation and revision of the manuscript. M.M., J.K. and J.T. wrote the original draft and coordinated the contributions of the other authors.

Data Availability Statement

Original data of this work are available upon reasonable request.

Credit Author Statement

Michael Meindlhumer: Conceptualization, Investigation, Data curation, Validation, Visualization, Writing – Original draft preparation. **Jakub Zalesak**: Investigation. **Werner Ecker**: Investigation, Data curation, Funding acquisition. **Martin Rosenthal**: Resources, Investigation. **Sven Niese**: Investigation. **Peter Gawlitza**: Investigation. **Hynek Hruby**: Conceptualization, Writing - Review & Editing. **Christian Mitterer**: Writing - Review & Editing. **Rotislav Daniel**: Conceptualization, Writing - Review & Editing, Funding acquisition, Project Administration Supervision. **Jozef Keckes**: Conceptualization, Original draft preparation, Funding acquisition, Supervision. **Juraj Todt**: Conceptualization, Original draft preparation.

Declaration of Competing Interest

None.

Acknowledgment

This work has been financially supported by the Christian Doppler Research Association. The financial support by the Austrian Federal Ministry of Science, Research and Economy and the National

Foundation for Research, Technology and Development is also gratefully acknowledged. The CzechNanoLab project LM2018110 funded by MEYS CR is gratefully acknowledged for the financial support of the measurements/sample fabrication at CEITEC Nano Research Infrastructure. Furthermore, the authors gratefully acknowledge the financial support within the scope of the COMET program in the K2 Center "Integrated Computational Material, Process and Product Engineering (IC-MPPE)" (Project No 859480). This program is supported by the Austrian Federal Ministries for Climate Action, Environment, Energy, Mobility, Innovation and Technology (BMK) and for Digital and Economic Affairs (BMDW), represented by the Austrian research funding association (FFG), and the federal states of Styria, Upper Austria and Tyrol. Special thanks are devoted to Gabriele Felber for the preparation of the synchrotron lamella, Andrea Bachmaier and Stefan Wurster for help with the TKD measurements and Nikolaus Jäger for scratch testing.

Appendix A. Supplementary data

Supplementary data to this article can be found online at https://doi.org/10.1016/j.matdes.2020.109023.

References

[1] A.J. Perry, Scratch adhesion testing of hard coatings, Thin Solid Films 107 (1983) 167–180, https://doi.org/10.1016/0040-6090(83)90019-6.
[2] J. Valli, A review of adhesion test methods for thin hard coatings, J. Vac. Sci. Technol. A Vacuum, Surfaces, Film. 4 (1986) 3007–3014. doi:https://doi.org/10.1116/1.573616.
[3] P.A. Steinmann, Y. Tardy, H.E. Hintermann, S. Diego, N. Aeronautics, Adhesion testing by the scratch test method : the influence of intrinsic and extrinsic parameters on the critical load, Thin Solid Films 154 (1987) 333–349.
[4] H. Ichimura, Y. Ishii, Effects of indenter radius on the critical load in scratch testing, Surf. Coatings Technol. 165 (2003) 1–7.
[5] S.J. Bull, Failure modes in scratch adhesion testing, Surf. Coatings Technol. 50 (1991) 25–32, https://doi.org/10.1016/0257-8972(91)90188-3.
[6] S.J. Bull, Failure mode maps in the thin film scratch adhesion test, Tribol. Int. 30 (1997) 491–498. doi:10.1016/S0301-679X(97)00012-1.
[7] B.D. Beake, A.J. Harris, T.W. Liskiewicz, Review of recent progress in nanoscratch testing, Tribol. - Mater. Surfaces Interfaces. 7 (2013) 87–96, https://doi.org/10.1179/1751584x13y.0000000037.
[8] B.D. Beake, V.M. Vishnyakov, A.J. Harris, Relationship between mechanical properties of thin nitride-based films and their behaviour in nano-scratch tests, Tribol. Int. 44 (2011) 468–475, https://doi.org/10.1016/j.triboint.2010.12.002.
[9] B. Bhushan, Nanotribology and nanomechanics, Wear. 259 (2005) 1507–1531, https://doi.org/10.1016/j.wear.2005.01.010.
[10] B. Bhushan, B.K. Gupta, M.H. Azarian, Nanoindentation, microscratch, friction and wear studies of coatings for contact recording applications, Wear. 181–183 (1995) 743–758, https://doi.org/10.1016/0043-1648(95)90191-4.
[11] X. Li, B. Bhushan, A review of nanoindentation continuous stiffness measurement technique and its applications, Mater. Charact. 48 (2002) 11–36, https://doi.org/10.1016/S1044-5803(02)00192-4.
[12] A. Kleinbichler, M.J. Pfeifenberger, J. Zechner, S. Wöhlert, M.J. Cordill, Scratch induced thin film buckling for quantitative adhesion measurements, Mater. Des. 155 (2018) 203–211, https://doi.org/10.1016/j.matdes.2018.05.062.
[13] M. Larsson, M. Olsson, P. Hedenqvist, S. Hogmark, Mechanisms of coating failure as demonstrated by scratch and indentation testing of TiN coated HSS, Surf. Eng. 16 (2000) 436–444, https://doi.org/10.1179/026708400101517350.
[14] G.A. Fontalvo, R. Daniel, C. Mitterer, Interlayer thickness influence on the tribological response of bi-layer coatings, Tribiology Int. 43 (2010) 108–112, https://doi.org/10.1016/j.triboint.2009.05.002.
[15] J.M. Lackner, W. Waldhauser, B. Major, L. Major, M. Kot, Plastic deformation in nanoscale multilayer materials - a biomimetic approach based on nacre, Thin Solid Films 534 (2013) 417–425, https://doi.org/10.1016/j.tsf.2013.03.025.
[16] P. Wiecinski, J. Smolik, H. Garbacz, K.J. Kurzydlowski, Microstructure and mechanical properties of nanostructure multilayer CrN/Cr coatings on titanium alloy, Thin Solid Films 519 (2011) 4069–4073, https://doi.org/10.1016/j.tsf.2011.01.183.
[17] M. Stefenelli, R. Daniel, W. Ecker, D. Kiener, J. Todt, A. Zeilinger, C. Mitterer, M. Burghammer, J. Keckes, X-ray nanodiffraction reveals stress distribution across an indented multilayered CrN–Cr thin film, Acta Mater. 85 (2015) 24–31, https://doi.org/10.1016/j.actamat.2014.11.011.
[18] P. Wieciński, J. Smolik, H. Garbacz, K.J. Kurzydłowski, Failure and deformation mechanisms during indentation in nanostructured Cr/CrN multilayer coatings, Surf. Coatings Technol. 240 (2014) 23–31, https://doi.org/10.1016/j.surfcoat.2013.12.006.
[19] R. Daniel, K.J. Martinschitz, J. Keckes, C. Mitterer, Texture development in polycrystalline CrN coatings : the role of growth conditions and a Cr interlayer, J. Appl. Phys. D. 42 (2009) 13, https://doi.org/10.1088/0022-3727/42/7/075401.
[20] R. Daniel, M. Meindlhumer, J. Zalesak, B. Sartory, A. Zeilinger, C. Mitterer, J. Keckes, Fracture toughness enhancement of brittle nanostructured materials by spatial heterogeneity: a micromechanical proof for CrN/Cr and TiN/SiOx multilayers, Mater. Des. 104 (2016) 227–234, https://doi.org/10.1016/j.matdes.2016.05.029.
[21] S. Brinckmann, G. Dehm, Nanotribology in austenite : plastic plowing and crack formation, Wear. 338–339 (2015) 436–440, https://doi.org/10.1016/j.wear.2015.05.001.
[22] S. Brinckmann, C.A.C. Fink, G. Dehm, Nanotribology in austenite : Normal force dependence 339 (2015) 430–435, https://doi.org/10.1016/j.wear.2015.04.023.
[23] M.K. Khan, M.E. Fitzpatrick, S.V. Hainsworth, A.D. Evans, L. Edwards, Application of synchrotron X-ray diffraction and nanoindentation for the determination of residual stress fields around scratches, Acta Mater. 59 (2011) 7508–7520, https://doi.org/10.1016/j.actamat.2011.08.034.
[24] N.X. Randall, The current state-of-the-art in scratch testing of coated systems, Surf. Coatings Technol. 380 (2019) 17, https://doi.org/10.1016/j.surfcoat.2019.125092.
[25] K. Holmberg, A. Laukkanen, H. Ronkainen, K. Wallin, S. Varjus, A model for stresses , crack generation and fracture toughness calculation in scratched TiN-coated steel surfaces, 254 (2003) 278–291.
[26] K. Holmberg, A. Laukkanen, H. Ronkainen, K. Wallin, S. Varjus, J. Koskinen, Tribological contact analysis of a rigid ball sliding on a hard coated surface. Part I: Modelling stresses and strains, Surf. Coatings Technol. 200 (2006) 3793–3809. doi:https://doi.org/10.1016/j.surfcoat.2005.03.040.
[27] S. Roy, E. Darque-Ceretti, E. Felder, F. Raynal, I. Bispo, Experimental analysis and finite element modelling of nano-scratch test applied on 40-120 nm SiCN thin films deposited on cu/Si substrate, Thin Solid Films 518 (2010) 3859–3865, https://doi.org/10.1016/j.tsf.2010.02.004.
[28] J. Keckes, R. Daniel, J. Todt, J. Zalesak, B. Sartory, S. Braun, J. Gluch, M. Rosenthal, M. Burghammer, C. Mitterer, S. Niese, A. Kubec, 30 nm X-ray focusing correlates oscillatory stress, texture and structural defect gradients across multilayered TiN-SiOxthin film, Acta Mater. 144 (2018) 862–873, https://doi.org/10.1016/j.actamat.2017.11.049.
[29] N. Jäger, S. Klima, H. Hruby, J. Julin, M. Burghammer, J.F. Keckes, C. Mitterer, R. Daniel, Evolution of structure and residual stress of a fcc / hex-AlCrN multi- layered system upon thermal loading revealed by cross-sectional X- ray nano-diffraction, Acta Mater. 162 (2019) 55–66, https://doi.org/10.1016/j.actamat.2018.09.031.
[30] M. Meindlhumer, N. Jäger, S. Spor, M. Rosenthal, J.F. Keckes, H. Hruby, C. Mitterer, R. Daniel, J. Keckes, J. Todt, Nanoscale residual stress and microstructure gradients across the cutting edge area of a TiN coating on WC co, Scr. Mater. 182 (2020) 11–15, https://doi.org/10.1016/j.scriptamat.2020.02.031.
[31] M. Meindlhumer, J. Zalesak, R. Pitonak, J. Todt, B. Sartory, M. Burghammer, A. Stark, N. Schell, R. Daniel, J.F. Keckes, M. Lessiak, A. Köpf, R. Weißenbacher, J. Keckes, Biomimetic Hard and Tough Nanoceramic Ti–Al–N Film with Self-Assembled Six-Level Hierarchy, Nanoscale, 2019https://doi.org/10.1039/C8NR10339A.
[32] D.P. Gruber, J. Todt, N. Wöhrl, J. Zalesak, M. Tkadletz, A. Kubec, S. Niese, M. Burghammer, M. Rosenthal, H. Sternschulte, M.J. Pfeifenberger, B. Sartory, J. Keckes, Gradients of microstructure , stresses and mechanical properties in a multi-layered diamond thin fi lm revealed by correlative cross-sectional, 144 (2019) 666–674. doi:https://doi.org/10.1016/j.carbon.2018.12.093.
[33] A. Zeilinger, J. Todt, C. Krywka, M. Müller, W. Ecker, B. Sartory, M. Meindlhumer, M. Stefenelli, R. Daniel, C. Mitterer, J. Keckes, In-situ observation of cross-sectional microstructural changes and stress distributions in fracturing TiN thin film during Nanoindentation, Sci. Rep. 6 (2016) 22670, https://doi.org/10.1038/srep22670.
[34] W. Ecker, J. Keckes, M. Krobath, J. Zalesak, R. Daniel, M. Rosenthal, J. Todt, Nanoscale evolution of stress concentrations and crack morphology in multilayered CrN coating during indentation : experiment and simulation, Mater. Des. 188 (2020) 108478, https://doi.org/10.1016/j.matdes.2020.108478.
[35] M. Stefenelli, J. Todt, A. Riedl, W. Ecker, T. Müller, R. Daniel, M. Burghammer, J. Keckes, X-ray analysis of residual stress gradients in TiN coatings by a Laplace space approach and cross- sectional nanodiffraction : a critical comparison research papers, J. Appl. Crystallogr. 46 (2013) 1378–1385, https://doi.org/10.1107/S0021889813019535.
[36] A. Kubec, S. Niese, M. Rosenthal, J. Gluch, M. Burghammer, P. Gawlitza, J. Keckes, A. Leson, Sub 25 nm focusing with a long working distance using multilayer Laue lenses, J. Instrum. 13 (2018). doi:https://doi.org/10.1088/1748-0221/13/04/C04011.
[37] J. Kieffer, D. Karkoulis, J.P. Conf, Related content PyFAI , a versatile library for azimuthal regrouping, (2013) 8–13. doi:https://doi.org/10.1088/1742-6596/425/20/202012.
[38] G. Ashiotis, A. Deschildre, Z. Nawaz, J.P. Wright, D. Karkoulis, F.E. Picca, J. Kieffer, The fast azimuthal integration Python library: PyFAI, J. Appl. Crystallogr. 48 (2015) 510–519, https://doi.org/10.1107/S1600576715004306.
[39] M. Bartosik, R. Daniel, C. Mitterer, I. Matko, M. Burghammer, P.H. Mayrhofer, J. Keckes, Cross-sectional X-ray nanobeam diffraction analysis of a compositionally graded CrNx thin film, Thin Solid Films 542 (2013) 1–4, https://doi.org/10.1016/j.tsf.2013.05.102.
[40] R. Daniel, K.J. Martinschitz, J. Keckes, C. Mitterer, The origin of stresses in magnetron-sputtered thin films with zone T structures, Acta Mater. 58 (2010) 2621–2633, https://doi.org/10.1016/j.actamat.2009.12.048.
[41] J. Almer, U. Lienert, R.L. Peng, C. Schlauer, M. Odén, Strain and texture analysis of coatings using high-energy x-rays, J. Appl. Phys. 94 (2003) 697. doi:10.1063/1.1582351.
[42] J. Pina, A. Dias, M. François, J.L. Lebrun, Residual stresses and crystallographic texture in hard-chromium electroplated coatings, Surf. Coatings Technol. 96 (1997) 148–162, https://doi.org/10.1016/S0257-8972(97)00075-3.
[43] Abaqus Unified FEA - SIMULIATM™ by Dassault Systèmes®, (n.d.). https://www.3ds.com/products-services/simulia/products/abaqus/ (accessed June 15, 2020)., (n.d.).

[44] S. Liu, J.M. Wheeler, J. Michler, X.T. Zeng, W.J. Clegg, Plastic flow at the theoretical yield stress in ceramic films, Scr. Mater. 117 (2016) 24–27, https://doi.org/10.1016/j.scriptamat.2016.02.008.
[45] A. Zeilinger, R. Daniel, M. Stefenelli, B. Sartory, L. Chitu, M. Burghammer, T. Schöberl, O. Kolednik, J. Keckes, C. Mitterer, Mechanical property enhancement in laminates through control of morphology and crystal orientation, J. Phys. D. Appl. Phys. 48 (2015) 9, https://doi.org/10.1088/0022-3727/48/29/295303.
[46] P. Wang, P. Ge, W. Bi, T. Liu, Y. Gao, Stress analysis in scratching of anisotropic single-crystal silicon carbide, Int. J. Mech. Sci. 141 (2018) 1–8, https://doi.org/10.1016/j.ijmecsci.2018.03.042.
[47] C. Greiner, Z. Liu, R. Schneider, L. Pastewka, P. Gumbsch, The origin of surface microstructure evolution in sliding friction, Scr. Mater. 153 (2018) 63–67, https://doi.org/10.1016/j.scriptamat.2018.04.048.
[48] X. Chen, R. Schneider, P. Gumbsch, C. Greiner, Microstructure evolution and deformation mechanisms during high rate and cryogenic sliding of copper, Acta Mater. 161 (2018) 138–149, https://doi.org/10.1016/j.actamat.2018.09.016.
[49] C. Haug, F. Ruebeling, A. Kashiwar, P. Gumbsch, C. Kübel, C. Greiner, Early deformation mechanisms in the shear affected region underneath a copper sliding contact, Nat. Commun. 11 (2020). doi:https://doi.org/10.1038/s41467-020-14640-2.
[50] L.A. Feigin, D.I. Svergun, Structure Analysis by Small-Angle X-Ray and Neutron Scattering, 1987.
[51] I. Petrov, P.B. Barna, L. Hultman, J.E. Greene, I. Introduction, Microstructural evolution during film growth, (2003) 117–128. doi:https://doi.org/10.1116/1.1601610.
[52] M.L. Suominen Fuller, R.J. Klassen, N.S. McIntyre, A.R. Gerson, S. Ramamurthy, P.J. King, W. Liu, Texture, residual strain, and plastic deformation around scratches in alloy 600 using synchrotron X-ray Laue micro-diffraction, J. Nucl. Mater. 374 (2008) 482–487, https://doi.org/10.1016/j.jnucmat.2007.10.015.
[53] K. Holmberg, A. Laukkanen, H. Ronkainen, K. Wallin, S. Varjus, J. Koskinen, Tribological contact analysis of a rigid ball sliding on a hard coated surface. Part II: Material deformations influence of coating thickness and young's modulus, Surf. Coatings Technol. 200 (2006) 3810–3823. doi:https://doi.org/10.1016/j.surfcoat.2005.03.041.
[54] A. Laukkanen, K. Holmberg, J. Koskinen, H. Ronkainen, K. Wallin, S. Varjus, Tribological contact analysis of a rigid ball sliding on a hard coated surface, part III: fracture toughness calculation and influence of residual stresses, Surf. Coatings Technol. 200 (2006) 3824–3844, https://doi.org/10.1016/j.surfcoat.2005.03.042.
[55] B.L. Boyce, X. Chen, J.W. Hutchinson, R.O. Ritchie, The residual stress state due to a spherical hard-body impact, Mech. Mater. 33 (2001) 441–454, https://doi.org/10.1016/S0167-6636(01)00064-3.
[56] B.L. Boyce, A. Mehta, J.O. Peters, R.O. Ritchie, A spatially-resolved synchrotron diffraction method for evaluating impact-induced residual stresses, J. Neutron Res. 12 (2004) 75–80, https://doi.org/10.1080/10238160410001734496.
[57] K. Holmberg, A. Laukkanen, H. Ronkainen, K. Wallin, Tribological analysis of fracture conditions in thin surface coatings by 3D FEM modelling and stress simulations, Tribol. Int. 38 (2005) 1035–1049, https://doi.org/10.1016/j.triboint.2005.07.028.
[58] S.J. Bull, E. G.-Berasetegui, An overview of the potential of quantitative coating adhesion measurement by scratch testing, Tribol. Int. 39 (2005) 99–114. doi:https://doi.org/10.1016/S0167-8922(06)80043-X.